Title: Identification of a Binding Site for Small Molecule Inhibitors Targeting Human TRPM4

Authors

Babatunde Ekundayo[1], Prakash Arullampalam[2], Christian E. Gerber[2], Anne-Flore Hämmerli[2], Sabrina Guichard[2], Mey Boukenna[2], Daniela Ross-Kaschitza[2], Martin Lochner[2], Jean-Sebastien Rougier[2], Henning Stahlberg[1]*, Hugues Abriel[2]*, and Dongchun Ni[1]

Affiliations

[1] Laboratory of Biological Electron Microscopy, IPHYS, SB, EPFL, and Dept. Fundamental Microbiology, Faculty of Biology and Medicine, UNIL, Cubotron, Rt. de la Sorge, 1015 Lausanne, Switzerland.

[2] Institute of Biochemistry and Molecular Medicine and Swiss National Centre of Competence in Research TransCure, University of Bern, Bern, Switzerland

* Corresponding authors: henning.stahlberg@epfl.ch, hugues.abriel@unibe.ch

Abstract:

Transient receptor potential (TRP) melastatin 4 (TRPM4) protein is a calcium-activated monovalent cation channel associated with various genetic and cardiovascular disorders. The anthranilic acid derivative NBA is a potent and specific TRPM4 inhibitor, but its binding site in TRPM4 has been unknown, although this information is crucial for drug development targeting TRPM4. We determined three cryo-EM structures of full-length human TRPM4 embedded in native lipid nanodiscs without inhibitor, bound to NBA, and a new anthranilic acid derivative, IBA. We found that the small molecules NBA and IBA were bound in a pocket formed between the S3, S4, and TRP helices and the S4-S5 linker of TRPM4. Our structural data and results from patch clamp experiments enable validation of a binding site for small molecule inhibitors, paving the way for further drug development targeting TRPM4.

Main text

Introduction

Transient receptor potential (TRP) ion channels, a superfamily of cation channels, play a crucial role in various physiological functions, including sensory perception, cellular homeostasis, and ion transport [1,2]. The potential of TRP channels as therapeutic targets for drug development is immense, given that mutations in the genes encoding these channels can lead to their dysfunction or dysregulation, implicating them in numerous diseases and genetic disorders [3,4]. This underscores the importance of our research in understanding the role of TRP ion channels, particularly TRPM4, and their potential as therapeutic targets for drug development.

The TRPM (melastatin-like transient receptor potential) sub-family member, TRPM4, is a calcium-activated non-selective monovalent cation channel. The voltage-dependent activation of TRPM4 by intracellular calcium drives a current due to monovalent cations flux such as Na^+ and K^+ through the channel, leading to plasma membrane depolarization facilitating, in many cell types, calcium uptake via other calcium-permeable channels [5,6]. TRPM4 activity regulates physiological processes such as cardiac conduction, smooth muscle contraction, insulin secretion, and immune responses [7–9]. Genetic defects in *TRPM4* are found in patients with inherited cardiac conduction disorders. Furthermore, alterations of TRPM4 function are linked to diabetes, hypertension, and cancer [10–16]. Thus far, several small molecules identified and developed as potent and selective TRPM4 inhibitors are used as research tools to investigate the potential of TRPM4 as a therapeutic target and are promising candidates for drug development [17]. These molecules include 9-phenanthrol, flufenamic acid and the anthranilic acid derivatives CBA (4-chloro-2-[2-(2-chloro-phenoxy)-acetylamino]-benzoic acid) and NBA (4-chloro-2-(2-(naphthalene-1-yloxy) acetamido) benzoic acid [18–21]. NBA and CBA are thus far the most selective and potent TRPM4 inhibitors reported; however, it remains unknown how these drugs bind and inhibit TRPM4

52 activity [19]. To facilitate drug development targeting TRPM4, detailed structural information
53 revealing the mode of binding these molecules to TRPM4 is essential.

54 Cryo-electron microscopy (cryo-EM) enabled the structure determination of several TRP
55 channels. It revealed the druggable sites in these channels by structure determination in the
56 presence of antagonists and drug molecules [3,17]. These structures have revealed different
57 drug-binding pockets around the TRP channels' transmembrane domains (TMD). For
58 example, the synthetic molecule icilin binds into a hydrophobic pocket of the Voltage Sensor
59 Like Domain (VSLD) in TRPM8 and the binding of the small molecule inhibitor NDNA (*N'*-
60 (3,4-dimethoxybenzylidene)-2-(naphthalen-1-yl)acetohydrazide) into the cavity between the
61 S1-S4 domain and pore domain of TRPM5 [22,23]. These two examples revealed different
62 drug-binding sites within the same subfamily of TRP channels. Interestingly, lipid molecules
63 can share binding sites with drug molecules and inhibit drug binding and activity, as
64 demonstrated in the binding of 2-ABP (2-aminoethyl diphenylborinate) into the VBP
65 (Vallanoid Binding Pocket) of TRPV2, which could be inhibited by binding an endogenous
66 cholesterol molecule [24].

67 Structures of detergent-isolated TRPM4 studied by cryo-EM have revealed the binding sites
68 of the cholesterol homolog CHS (Cholesteryl Hemisuccinate) used to purify TRPM4,
69 suggesting potential endogenous cholesterol binding sites [25–28]. However, to date, no
70 structures of TRPM4 have been reported to be bound to specific inhibitors. The addition of
71 CHS required for stabilizing TRPM4 during detergent isolation could potentially occlude
72 drug-binding sites, posing a challenge in understanding TRPM4 inhibition. To address this
73 problem, we have isolated TRPM4 in its native lipid environment using SMA (Styrene Maleic
74 Anhydride) nanodiscs and determined its high-resolution structure in the presence and
75 absence of the small molecules NBA and a new derivative IBA (4-chloro-2-[2-(3-
76 iodophenoxy)-acetylamino]-benzoic acid) which has a similar potency to NBA (**Figure 1;**
77 **Figure 2a-c and Supplementary Fig. 1-8; see method section for IBA synthesis**) [29].
78 These structures reveal the mode of binding and inhibition of two potent and specific TRPM4

79 inhibitors, paving the way for future drug development and facilitating further investigations

80 of TRPM4 as a therapeutic target for treating related maladies.

81 **Results**

82 **Structures of HsTRPM4 in its native lipid environment**

83 We determined cryo-EM structures of full-length human TRPM4 in endogenous lipid
84 nanodiscs in apo ($HsTRPM4_{apo}$), IBA ($HsTRPM4_{IBA}$), and NBA ($HsTRPM4_{NBA}$) bound states
85 at overall resolutions of 3.7, 3.6, and 4.5 Å respectively (**Figure 1; Figure 2;**
86 **Supplementary Fig. 4-8; Supplementary Table 1**). All structures obtained were identical to
87 previously determined cryo-EM structures of TRPM4 in detergent micelles and reconstituted
88 nanodiscs [25–28]. However, we found that in native nanodiscs, densities for the cytosolic
89 regions of TRPM4 are poorly resolved compared to previously determined structures,
90 resulting in lower-resolution 3D reconstructions in these regions, which could be a result of
91 TRPM4 solubilization using SMA. This effect was more pronounced in the cytosolic N-
92 terminal TRPM homology regions 1 and 2 (MHR1/ 2), with the density in these regions much
93 less defined (**Supplementary Fig. 1c; Supplementary Fig. 2a and b**). Therefore, 3D
94 reconstructions could not be obtained for these regions (**Supplementary Fig. 2; 4- 6**).
95 These results suggest that SMA solubilization results in a less stable TRPM4 structure,
96 which could result from the differences in lipid composition or binding compared with
97 structures of TRPM4 in detergent micelles and reconstituted nanodiscs. Indeed, examination
98 of the TMD revealed that although the structural arrangement of the transmembrane helices
99 was identical, the lipid arrangement was strikingly different from previously determined
100 TRPM4 structures [25–28]. Notably, the published structure of HsTRPM4 in a reconstituted lipid
101 nanodisc, as well as cryo-EM density maps of detergent-solubilized human and mouse
102 Trpm4 from this study, revealed ordered densities for annular phospholipids and three CHS
103 molecules, one of which (CHS-2) occludes the drug binding site (**Supplementary Fig. 2 and**
104 **3; Supplementary Table 2)** [26].

105 On the other hand, in our structures, ordered densities for annular lipids are markedly
106 reduced, with primarily three densities for cholesterol molecules bound to TRPM4 observed
107 (**Figure 1a-d; Supplementary Fig. 2a and b**). Of the three, two cholesterol molecules

108 (CHR-1 and CHR-2) bind in similar positions to CHS molecules in a previous structure in a
109 reconstituted nanodisc (**Figure 1e-f; Supplementary Fig. 2a and b**). One of these
110 molecules (CHR-1) interacts with the S6 helix close to the channel pore, and another (CHR-
111 2) in a pocket formed between S3 and S4 helices and the S4-S5 linker equivalent to the VBP
112 of TRPV2; however, the density for this cholesterol molecule is weaker compared to CHR-1,
113 suggesting lower occupancy (**Figure 1e-f**). The third cholesterol molecule (CHR-3) in our
114 structures binds between the S5 and S2 helix from an adjacent protomer differing from the
115 previously reported position of CHS at the pre-S1 elbow (**Supplementary Fig. 2a-c**). The
116 presence of less density for annular lipids in the native nanodiscs was an essential factor
117 that enabled the assignment of density for the drugs in the HsTRPM4$_{IBA}$ and HsTRPM4$_{NBA}$
118 structures (**Fig. 2d-i**; **Supplementary Fig. 8**).

119 **The binding site of the small molecule inhibitors NBA and IBA in HsTRPM4**

120 Analysis of the HsTRPM4$_{IBA}$ and HsTRPM4$_{NBA}$ structures revealed discrete densities for the
121 IBA and NBA molecules located at the periphery of the inner membrane leaflet in the pocket
122 formed between S3 and S4 helices, S4-S5 linker, and TRP helix (**Figure 2d-f**). The
123 presence of the ligands in this pocket suggests that these ligands can displace the
124 endogenous cholesterol molecule (CHR-2) present in the HsTRPM4apo structure, which is
125 possibly not tightly bound as judged by the weaker density map for this molecule compared
126 to other bound cholesterol molecules (**Figure 1e and f)**. Ligand binding induces only very
127 subtle conformational changes in the structure of HsTRPM4, with the overall structures
128 remaining broadly similar (**Figure 2g and h**). The HsTRPM4 ion conduction pore is also in
129 the closed state in all three structures; however, subtle changes in pore diameter are
130 observed in the IBA-bound structure, although it remained closed (**Figure 2i**). In this study,
131 exogenous calcium was not added to the SMA-extracted TRPM4 samples used for cryo-EM
132 because adding divalent ions destabilizes SMA nanodiscs [29]. However, our cryo-EM density
133 maps of TRPM4 in native nanodiscs revealed a strikingly apparent density in the calcium-
134 binding site as observed in structures of detergent-extracted human and mouse TRPM4

135 supplemented with Ca^{2+}. Indeed, upon fitting a previously determined structure of calcium-
136 bound TRPM4 into our cryo-EM map of SMA-extracted TRPM4, we observe that the calcium
137 ion together with its interacting residues Glu828, Gln831, Asp 868, and Arg905 fit very well
138 into our cryoEM density of SMA extracted TRPM4 similar to cryoEM density maps of calcium
139 supplemented detergent isolated TRPM4 which were reproduced in this study
140 (**Supplementary Fig. 9**). Indeed, this suggests the binding of endogenous Ca^{2+} ions in the
141 SMA extracted TRPM4. Still, we cannot rule out the possibility of other endogenously
142 derived ions occupying the binding site. Nonetheless, the occupation of the calcium-binding
143 site in our structures did not result in an open state of the channel like previously described
144 in calcium-bound TRPM4 structures.

145 Both IBA and NBA share a common anthranilic acid moiety but differ in that NBA possesses
146 an additional ring of its naphthalene substituent, making it bulkier and more hydrophobic
147 than the smaller 3-iodophenyl ring of IBA (**Figure 2e and f, Supplementary Fig. 8**). The
148 additional ring of the naphthalene substituent of NBA was an important fiducial marker for
149 the overall placement of the ligands in the density maps. In both $HsTRPM4_{IBA}$ and
150 $HsTRPM4_{NBA}$ structures, the hydrophilic anthranilic acid moiety containing acidic, amide, and
151 chloride groups faces towards the cytosol interacting with charged amino acid side chains
152 from TRPM4 (**Figure 3a and b**). Notably, the anthranilic acid moiety interacts with His908
153 from the S4 helix, Tyr1057, Gln1061, and Arg1064 from the TRP helix, as well as with
154 Ser924 from the S4-S5 linker, and Ser863 from the S3 helix in both structures (**Figure 3a**
155 **and b**). These interactions between the anthranilic acid moiety and residues of TRPM4
156 reveal the chemical basis behind the specific binding of the anthranilic acid derivatives to
157 TRPM4.

158 NBA and IBA have a similar potency for TRPM4 inhibition, possibly by making additional
159 unknown interactions in the binding pocket (**Figure 2a-c**). Our structures show that the
160 naphthalene substituent and the 3-iodophenyl ring of NBA and IBA bind into a hydrophobic
161 pocket between the S3 and S4 helices of TRPM4 (**Figure 3c and d; Supplementary Fig.**

162 **7d and e**), making hydrophobic interactions with the residues that decorate this pocket,
163 including Val901, Val904 and Leu907 (**Figure 3c and d**). Therefore, these structures reveal
164 a rationale for the potency and specificity of NBA and IBA and pave the way for designing
165 chemical modifications of these molecules to enable increased targeting of the binding
166 pocket to develop more potent and specific inhibitors.

167 **Validation of the NBA and IBA binding site in HsTRPM4**

168 To disrupt the drug-protein interactions in the hydrophilic region of the drug binding site, we
169 introduced the HsTRPM4 mutations Ser863Ala (S863A), His908Ala (H908A), Ser924Ala
170 (S924A), Lys925Ala (K925A), Tyr1057Ala (Y1057A), Gln1061Ala (Q1061A), Arg1064Ala
171 (R1064A), Arg1064Gly (R1064G), Arg1064Ser (R1064S), and the double variant
172 Ser863Ala/Ser924Ala (S863A/S924A). Additional Val901Trp (V901W) and Val904Trp
173 (V904W) are space-filling mutations that disrupt the hydrophobic pocket. These mutations
174 were introduced to reduce the drug's inhibitory effect compared to wildtype HsTRPM4
175 (**Figure 3a-d**). First, the expression of the different variants was investigated using the
176 western blot approach (**Supplementary Fig. 10**). Only Ser863Ala and Gln1061Ala variants
177 showed a significantly reduced expression compared to the wildtype channel
178 (**Supplementary Fig. 10b**). In parallel, functional experiments revealed that after activation
179 of the HsTRPM4 function by adding a solution with a concentration of 300 µM of free
180 calcium, almost all variants displayed a significant reduction in the sodium current of the
181 calcium-activated HsTRPM4 channel except Ser863Ala, Ser924Ala, Arg1064Ala, and
182 Arg1064Gly quantify at a membrane voltage of +100 mV (**Figure 3e-f, Supplementary Fig.
183 12**). Due to the reduction of activation in these mutants and the proximity of these residues
184 in the NBA binding site to the calcium-binding site **(Figure 4a**), we wondered if this decrease
185 in function observed may be due to an alteration of the calcium sensitivity of those variants**.**
186 The calcium sensitivity curves performed on some loss-of-function HsTRPM4 variants
187 (Val904Trp, Tyr1057Ala, Gln1061Ala, Arg1064Ser, and the double variant Ser863Ala/
188 Ser924Ala) show that the different EC_{50s} for calcium are not higher compared to wildtype

189 HsTRPM4 suggesting that this decrease of function is not due to a reduction of calcium
190 sensitivity **(Figure 4b; Supplementary Fig. 13a).** On the contrary, the different EC_{50s} of the
191 variants are smaller than the wildtype EC_{50}, suggesting an increase in calcium sensitivity
192 **(Figure 4b; Supplementary Fig. 13a).** Following those experiments and knowing that the
193 inhibitory effect mediated by NBA will be investigated on these variants in the presence of
194 calcium (to activate them), control experiments were performed using HsTRPM4 wildtype
195 channels to explore the potential influence of NBA on calcium sensitivity. As for the variants,
196 the results suggest that NBA does not decrease the calcium sensitivity of the wildtype
197 channels (**Figure 4b; Supplementary Fig. 13b**). The absence of a decrease of the calcium
198 sensitivity in the presence of NBA and amino acid modifications led us to perform the final
199 experiment investigating the consequences of modifying those amino acids on the inhibitory
200 effect mediated by NBA. As a proof of concept, the mutations Ser863Ala, Val901Trp,
201 His908Ala, Ser924Ala, Arg1064Ala, Arg1064Gly, and the double variant Ser863Ala/
202 Ser924Ala were investigated. Compared to wildtype HsTRPM4, NBA dose-effect curves on
203 single variants of the HsTRPM4 channel show a drastic increase (up to one log of
204 difference) of the IC_{50s} for the NBA, suggesting a decreased efficiency of inhibition by NBA
205 (**Figure 5a**). Compared to the wildtype construct, but also to single amino acid variant
206 Ser863Ala and Ser924Ala, a more pronounced decrease in the efficiency of NBA of up to
207 two logs of difference is observed in the presence of the double mutation Ser863Ala/
208 Ser924Ala (**Fig. 5a,c, and d; Supplementary Figure 14**). In addition, a control experiment
209 was performed using a mutant of HsTRPM4 linked to cardiac dysfunction, which has already
210 been reported in the literature: the mutant HsTRPM4 T677I [30]. This variant was selected
211 based on its presence outside the putative NBA binding pocket and because this point
212 mutation did not alter the biophysical properties of channels [30]**.** This mutation did not alter
213 the IC_{50} of the NBA, as observed with the NBA binding pocket variants (**Figure 5e and f**).
214 Overall, these data strongly support the notion that those amino acids of HsTRPM4 are part
215 of the binding pocket for NBA or IBA, as determined by our cryo-EM structures.

216 **Discussion**

217 We have utilized cryo-EM to determine the high-resolution structures of HsTRPM4 bound to
218 specific inhibitors. Importantly, we find that using SMA to isolate HsTRPM4 in its
219 endogenous lipid nanodisc was necessary to assign densities for the inhibitor molecules,
220 which electrophysiology experiments could further validate. This finding supports the
221 relevance of previous attempts to isolate TRPM4 in its native lipid environment but,
222 unfortunately, yielded lower-resolution structures [31]. High-resolution structures of TRPM4
223 have previously been determined in detergent micelles and in reconstituted lipid nanodiscs,
224 both of which require detergent isolation of the protein from the cell and, by so doing,
225 introduce artifacts to the lipid environment of the protein. An essential factor is that the
226 added CHS, to maintain protein stability in detergent extraction, binds in specific sites in the
227 protein, which may or may not represent actual cholesterol-binding sites. We observed
228 apparent differences in the binding arrangement of annular lipids to TRPM4 from the
229 structural data when isolated with SMA. Most striking is that a CHS molecule completely
230 occupies the drug binding site, suggesting that obtaining a structure or performing
231 biochemical experiments with detergent-CHS isolated protein and these inhibitors does not
232 represent the endogenous scenario. Indeed, identifying the inhibitor binding site was
233 ambiguous in our previous attempts to determine the structure of detergent-isolated TRPM4
234 in a complex with NBA or IBA. This finding also shows the importance of the composition
235 and binding arrangement of the lipid annulus to the function and inhibition of the target
236 membrane protein. This study shows that using SMA would be advantageous for the
237 structure determination of drugs with membrane proteins, particularly in cases where the
238 drug binds in the TMD exposed to lipid molecules.

239 During the revision of this work, another paper was published, which revealed the
240 importance of temperature in modulating the structure of detergent-extracted TRPM4. More
241 precisely, at the warm temperature of 37°C, TRPM4 was shown to undergo structural
242 rearrangements, particularly in MHR1/2 domains of the ICD; interestingly, this region is also

243 flexible and poorly resolved in our structures, which could suggest an interplay of the lipid
244 environment with the temperature-induced structural movement [32]. Furthermore, the binding
245 site of the allosteric modulator DVT was also shown to change in a temperature-dependent
246 manner, leading to channel opening via the relative movement of the TRP helix to S1-S4
247 helices. This movement of the TRP helix is required for the activation of the TRPM2 channel
248 and is also required for desensitization of the TRPM8 channel [32,33,34]. These findings reveal
249 the important role of TRP helix movement in regulating the channel pore of the TRPM
250 subfamily. Based on our results and these previous studies, we propose that the binding of
251 NBA or IBA to TRPM4 may restrict the movement of the TRP helix, maintaining the TRPM4
252 channel pore in a closed state even in the presence of activation stimuli (**Figure 6**). The role
253 of the bound cholesterol molecule in the same pocket remains unclear. This cholesterol
254 could also regulate channel function in response to changes in the membrane environment.

255 A major limitation in our study is that we could not determine structures of SMA-extracted
256 TRPM4 in the presence of exogenous Ca^{2+} ions, as the addition of calcium destabilizes SMA
257 nanodiscs. Although we did observe density in the calcium-binding site, we cannot rule out
258 an effect or interrelation between the binding of Ca^{2+} ions and NBA or IBA. Moreover, we did
259 not observe decreases in calcium sensitivity in the presence of NBA, but the implications of
260 which remain unclear (**Figure 4**). However, other published structures of TRPM4 in the
261 presence and absence of Ca^{2+} ions reveal that the NBA or IBA binding site and residues
262 involved in the interaction between TRPM4 and NBA or IBA remain accessible for binding of
263 a CHS molecule in both states suggesting this pocket is accessible for binding of the
264 inhibitors in both states [26].

265 Our study has identified a binding pocket for inhibiting TRPM4 by the anthranilic acid
266 derivatives (**Figure 2d -f**). These drugs bind in a pocket between S3 and S4 helices, S4-S5
267 linker, and TRP helix. However, detailed insights into the mechanism of inhibition will require
268 structure determination of TRPM4 in its open state, which has been elusive. Adding Ca^{2+}
269 ions is insufficient to obtain the open state with purified TRPM4 in lipid nanodiscs. Still, the

presence of a membrane potential may be necessary. In the future, we will seek to address this by studying TRPM4 in lipid vesicles. Nonetheless, identifying a binding pocket for TRPM4 inhibitors presents a significant milestone towards further developing new potent and even more specific drugs targeting the TRPM4 ion channel for therapeutic intervention.

Acknowledgments

This work was supported by the Swiss National Science Foundation (SNF Grants CRSII5_177195 and the NCCR TransCure (185544)). We thank Emiko Uchikawa, Sergey Nazarov, and members of the DCI, Lausanne from EPFL, UNIL, and UNIGE for their support. We also thank Kelvin Lau, Florence Pojer, Laurence Durrer, and Soraya Quinch, the PTPSP at EPFL, for their support with protein expression.

Author Contributions Statement

HS and HA conceptualized the project. BE and DN performed cryo-EM sample preparation and structure determination with support from the DCI, Lausanne. PA, AH, SG, DRK, and MB performed biochemistry and patch clamp experiments. CEG. and ML designed the target molecule IBA and synthesis. CEG. performed the synthesis of NBA and IBA. Project administration and supervision was done by BE and JSR. BE wrote the original draft. Manuscript review & editing were done by DN, BE, JSR, ML, HA, and HS. HS and HA acquired funding. All authors read and approved the manuscript.

Competing Interests Statement

The authors declare no competing interests.

292 **Supplementary Table 1**

Data collection and processing	HsTRPM4apo (EMD-19057) (PDB 8RCR)	$HsTRPM4_{IBA}$ (EMD-19061) (8RCU)	$HsTRPM4_{NBA}$ (EMD-19069) (PDB 8RD9) (EMD-19060, local)
Nominal Magnification	165kx	165kx	165kx
Voltage (kV)	300	300	300
Recorded Micrographs	6 429	7 500	11 851
Electron exposure (e–/Å2)	50	50	50
Defocus range (μm)	0.8-2.5	0.8-2.5	0.8-2.5
Pixel size (Å)	0.726	0.726	0.726
Symmetry imposed	C4	C1/C4	C4
Initial particle images (no.)	1 719 323	1 149 090	1 805 182
Final particle images (no.)	16 308	20 345	15 954
Map resolution (Å)	3.67	3.59	4.50
FSC threshold	0.143	0.143	0.143
Map resolution range (Å)	30-3.3	30-3.2	30-3.6
Map sharpening B factor (Å2)	-69.7	-52.2	-108.1
Refinement			
Initial model used (PDB code)	6BQV	6BQV	6BQV
Model composition Non-hydrogen atoms Protein residues Ligands	 8 2420 CHR: 12	 9 2420 IBA: 4 CHR: 8	 8 2422 NBA: 4 CHR: 8
B factors ($Å^2$) Protein Ligand	 41.23/251.46/135.21 63.19/103.12/79.00	 0.00/93.44/38.86 15.44/136.15/47.75	 142.10/427.50/239.20 20.00/33.04/22.07
R.m.s. deviations Bond lengths (Å) Bond angles (°)	 0.012 (146) 0.801 (7)	 0.003 (0) 0.721 (0)	 0.004 (0) 0.925 (10)
Validation MolProbity score Clashscore Poor rotamers (%)	 1.93 14.67 0.00	 2.04 16.76 0.19	 2.23 24.33 0.05
Ramachandran plot Favored (%) Allowed (%) Disallowed (%)	 96.16 3.71 0.13	 95.49 4.34 0.17	 94.82 4.76 0.42

293

294 **Supplementary Table 1 | Cryo-EM data collection, refinement, and validation statistics**

295 **for SMA solubilized HsTRPM4 samples.**

296

297 **Supplementary Table 2**

Data collection and processing	HsTRPM4+Ca^{2+}	HsTRPM4+NBA+Ca^{2+}	MmTRPM4+Ca^{2+}
Nominal Magnification	96kx	96kx	165kx
Voltage (kV)	300	300	300
Recorded Micrographs	11 877	10 219	8 313
Electron exposure (e–/Å2)	40	40	60
Defocus range (μm)	0.8-2.5	0.8-2.5	0.8-2.5
Pixel size (Å)	0.83	0.83	0.726
Symmetry imposed	C4	C4	C4
Initial particle images (no.)	4 430 540	2 774 028	4 340 237
Final particle images (no.)	128 316	40 061	100 227
Map resolution (Å)	3.04	2.98	2.87
FSC threshold	0.143	0.143	0.143
Map resolution range (Å)	30-2.6	30-2.5	30-2.5

298

299 **Supplementary Table 2 | Cryo-EM data collection for DDM/CHS solubilized HsTRPM4**

300 **and MmTRPM4 samples.**

301

302

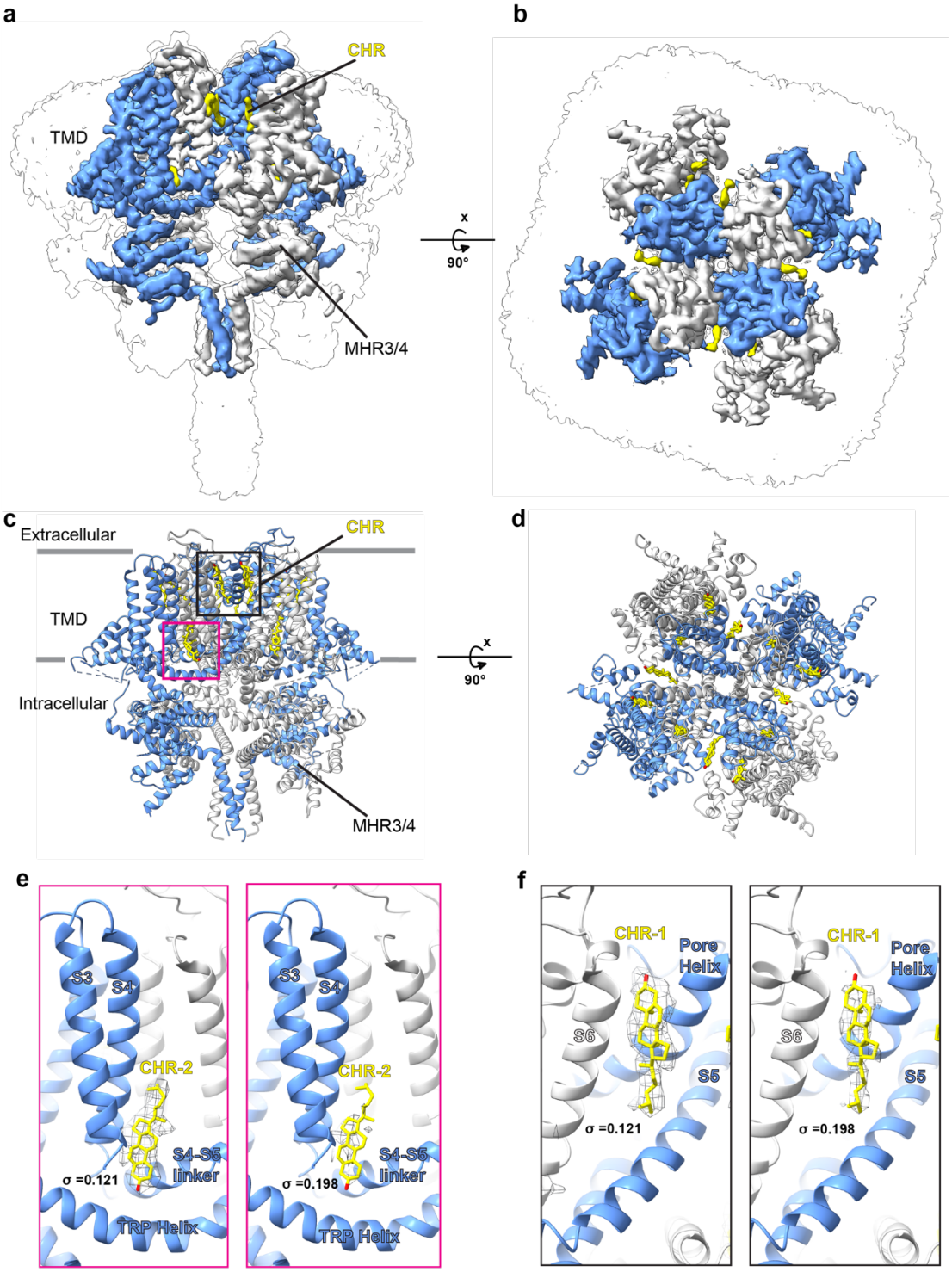

303

304 **Figure 1**: Overall structure of HsTRPM4$_{apo}$ in native lipid nanodiscs. (a and b) Two views

305 of the cryo-EM densities of HsTRPM4$_{apo}$ in surface representation. Alternating

306 protomers of TRPM4 are shown in blue and white. (c and d) Cartoon representation

307 of the HsTRPM4$_{apo}$ corresponding to the cryo-EM densities in a and b. The positions

308 of bound cholesterol molecules (CHR) are indicated. The black box indicates the
309 positions of CHR-1 and CHR-3, as shown in yellow. In contrast, the pink box
310 indicates the position of CHR-2. (e) Cryo-EM density in mesh representation for
311 CHR-2 (f) Cryo-EM density in mesh representation for CHR-1. In e and f, the density
312 threshold level is indicated by σ.
313

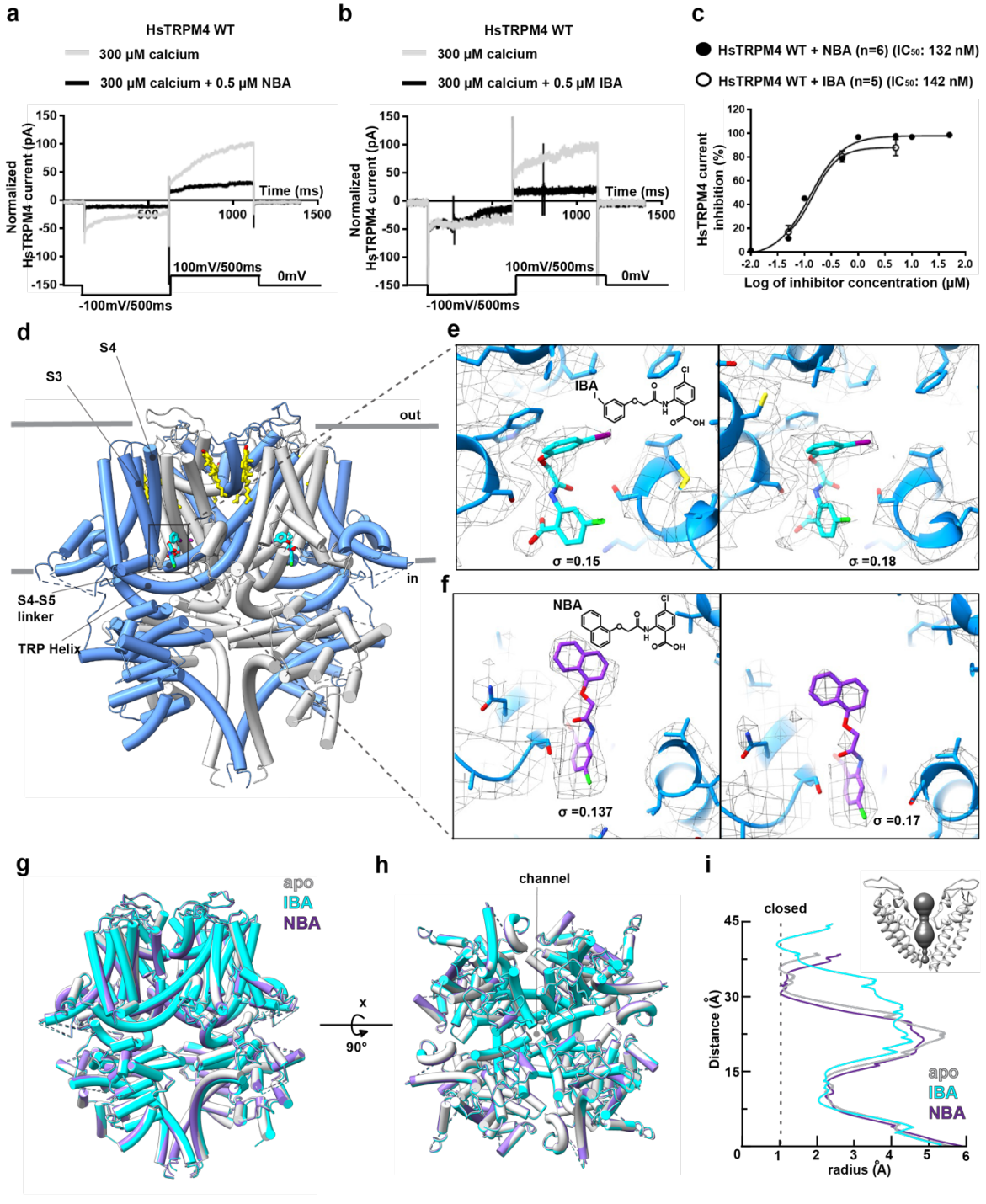

Figure 2: Structures of HsTRPM4$_{NBA}$ and HsTRPM4$_{IBA}$. (a) Representative sodium current of the calcium-activated HsTRPM4 wildtype (WT) channel in the presence of a solution with 300 µM of free calcium (grey line) and in the presence of a solution with 300 µM of free calcium with 0.5 µM of NBA (black line). (b) in the presence of a solution with 300 µM of free calcium (grey line) and in the presence of a solution with

300 μM of free calcium with 0.5 μM of IBA (black line). (c) NBA and IBA dose-response curves of wildtype (WT). (n): number of cells. (d) The structure of inhibitor-bound HsTRPM4 with box and dashed lines indicating the inhibitor binding site. (e and f) Zoom-in of IBA and NBA with the cryo-EM density in mesh representation at two different density threshold levels as indicated by σ. (g and h) Superimposition of $HsTRPM4_{apo}$ in light grey, $HsTRPM4_{NBA}$ in purple and $HsTRPM4_{IBA}$ in cyan. Two views of the structures are shown. (i) Pore radius for $HsTRPM4_{apo}$, $HsTRPM4_{NBA}$ and $HsTRPM4_{IBA}$, all calculated using MOLE. In the top right corner are the pore-forming helices in $HsTRPM4_{apo}$. The pore profile is shown as a space-filling model (grey).

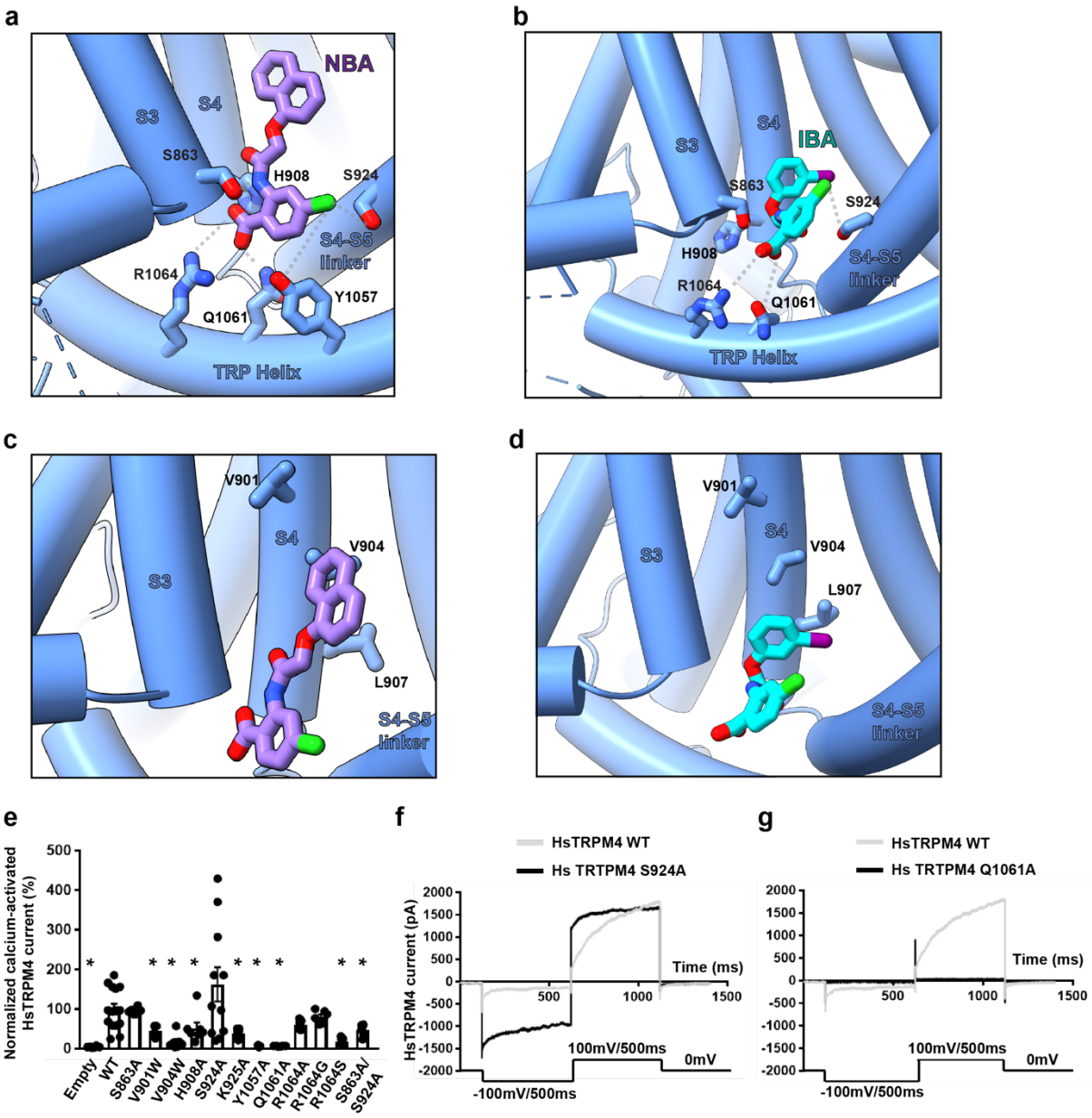

Figure 3: Amino acid interactions in the drug binding pocket. (a) Amino acid residues of HsTRPM4 involved in interactions with the anthranilic acid moiety of NBA (in purple) and (b) IBA (cyan) are shown. (c) Amino acid residues of HsTRPM4 involved in hydrophobic interactions with NBA (in purple) and (d) IBA (in cyan) are shown. (e) Graphical plot of normalized recorded sodium current of the calcium-activated HsTRPM4 channel for the wildtype (WT) and HsTRPM4 variants. (*) represents the p-value < 0.05 compared to the wildtype condition. At least 5 cells per condition have been recorded. (f and g) Representative traces of wildtype (WT) and variants sodium currents of the calcium-activated HsTRPM4 channels: S924A and Q1061A. Sodium currents of the calcium-

activated HsTRPM4 variant channels are generally smaller than WT currents, as depicted in Figure 3e, due to the amino acid alteration.

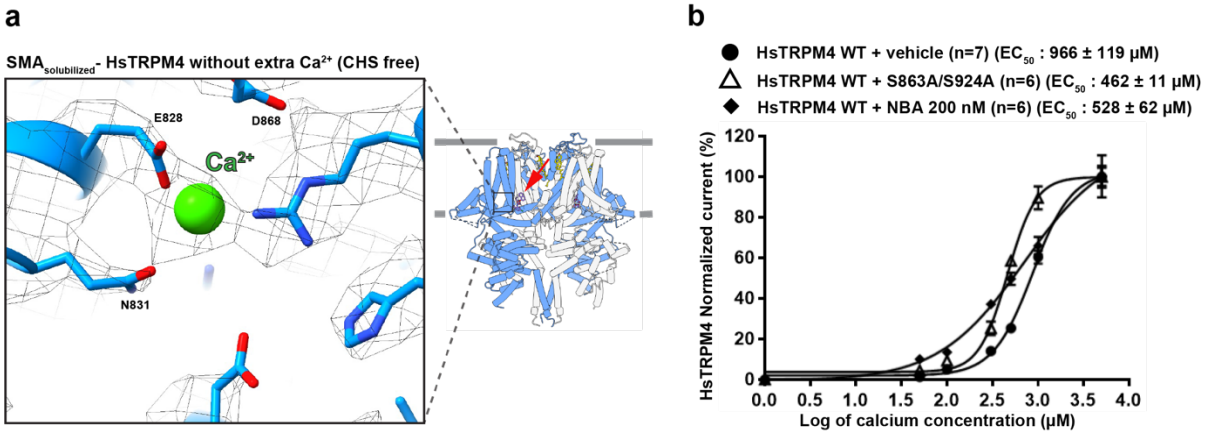

Figure 4: Calcium sensitivity of TRPM4 variants. (a) Zoom-in of the calcium-binding site with the cryo-EM density in mesh representation. The inhibitor binding site is also indicated with a red arrow. (b) Normalized calcium sensitivity curves for wildtype (WT) HsTRPM4 and loss-of-function HsTRPM4 variant S863A/S924A, and the effect of a solution containing the compounds NBA (200 nM) on this calcium sensitivity. (n): number of cells.

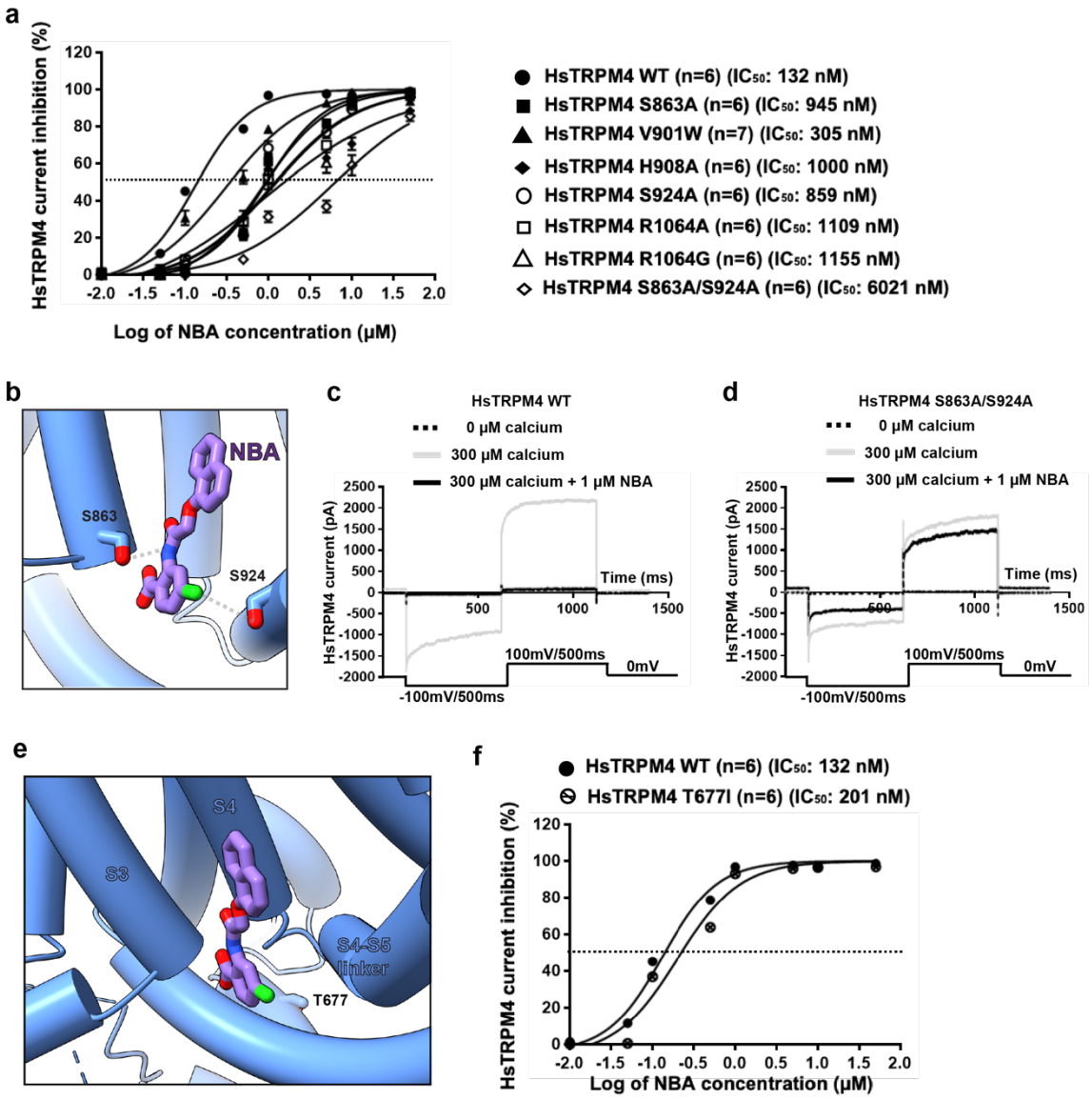

Figure 5: Effect of HsTRPM4 variants on NBA inhibition. (a) NBA dose-response curves of wildtype (WT) and variants of the predicted binding pocket of the HsTRPM4 channel, as a function of the decadic logarithm of the NBA concentration. (n): number of cells. (b) Locations of S863 and S924 in the drug binding pocket (c and d) Representative traces of wildtype (WT) and variant HsTRPM4 sodium currents: S863A/S924A in the absence of calcium (dotted black line), in the presence of a solution with a concentration of 300 µM of free calcium (grey line) and in the presence of a solution with a concentration of 300 µM of free calcium and 1 µM of NBA (black line). (e) Representation of the T677I variant located outside of the drug binding pocket of the TRPM4 channel. (f) NBA dose-response curves of wildtype (WT) and a T677I variant. (n): number of cells.

362

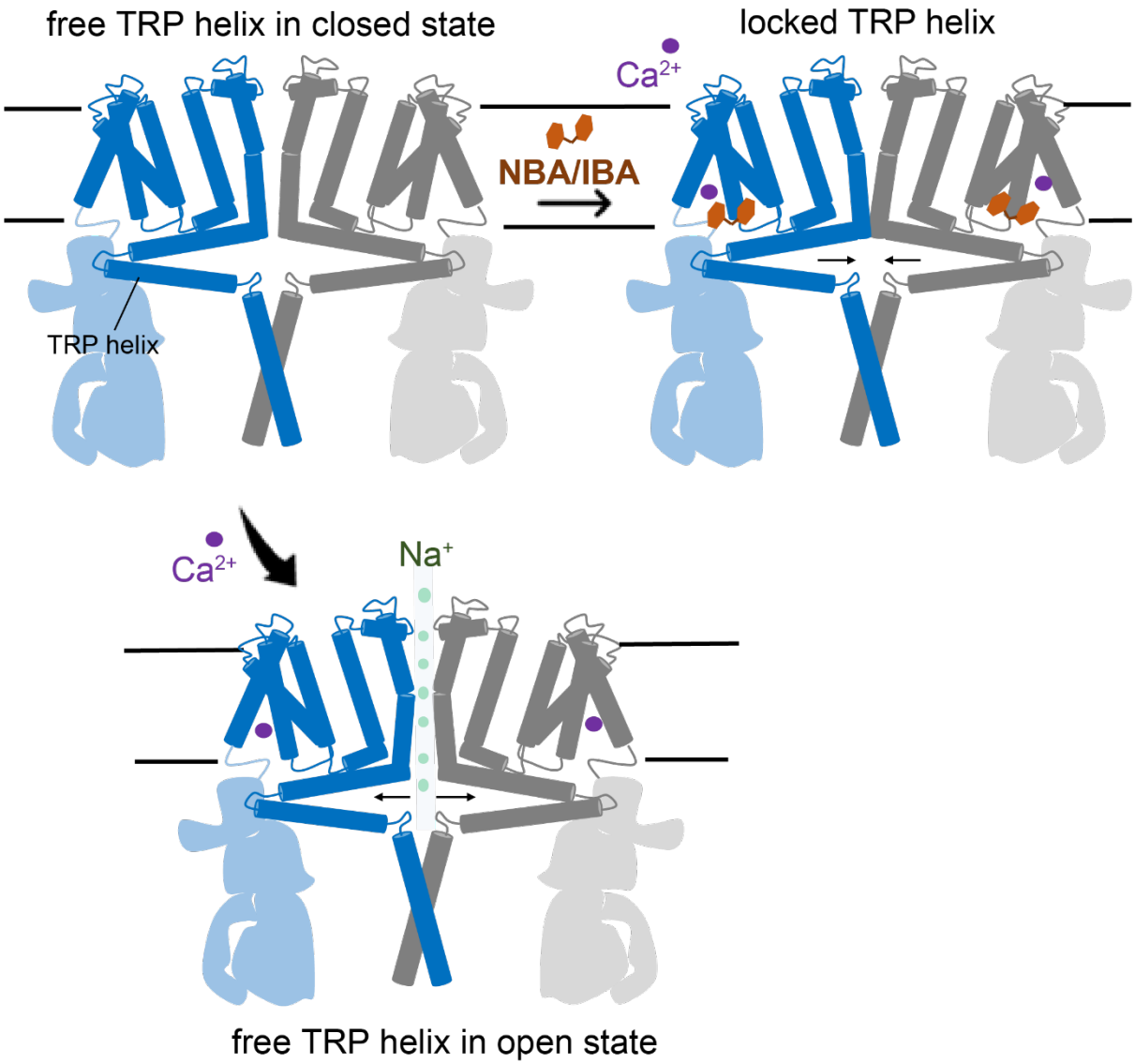

363

364 **Figure 6**: Proposed inhibition mechanism. The binding of anthranilic acid drugs such as

365 NBA, CBA, and IBA in the TRPPM4 drug binding site leads to channel blocking, possibly by

366 restricting the movement of the TRP helix, thereby preventing channel opening upon calcium

367 activation.

368

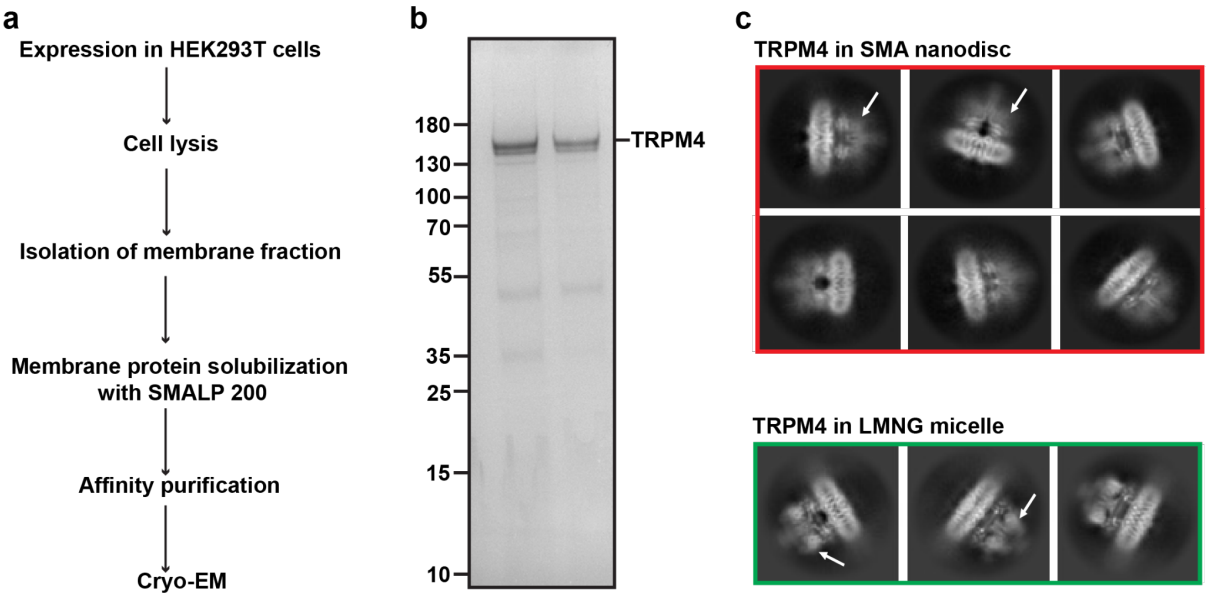

Supplementary Fig. 1: Purification of TRPM4 in SMA-extracted native lipid nanodiscs. (a) Biochemical workflow for isolating and purifying HsTRPM4 in native lipid nanodiscs using SMA (SMALP-200). (b) SDS-PAGE gel of purified HsTRPM4 following affinity purification. (c) Cryo-EM 2D class averages of TRPM4 in SMA-extracted native lipid nanodiscs and LMNG detergent micelles. White arrows indicate the positions of MHR1/2 in the TRPM4 2D classes.

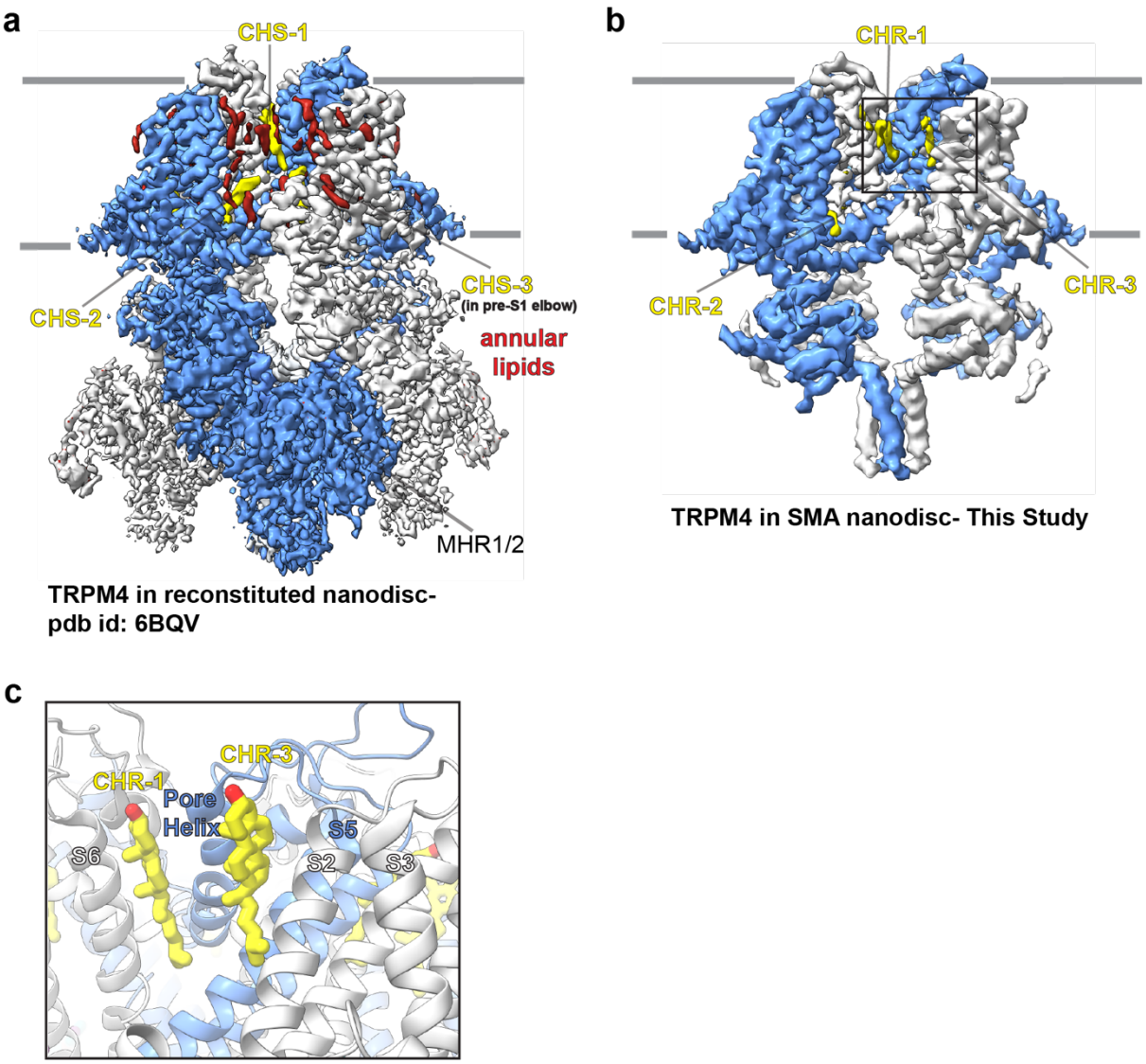

Supplementary Fig. 2: Comparison of the annular lipid environment between the cryo-EM maps of HsTRPM4 in reconstituted lipid nanodiscs [26] (a) and SMA-extracted native lipid nanodiscs (b). CHS represents cholesteryl hemisuccinate in (a), and CHR represents cholesterol in (b). (c) The location of CHR-1 and CHR-3 is shown from the cryo-EM structure of HsTRPM4 in native lipid nanodiscs.

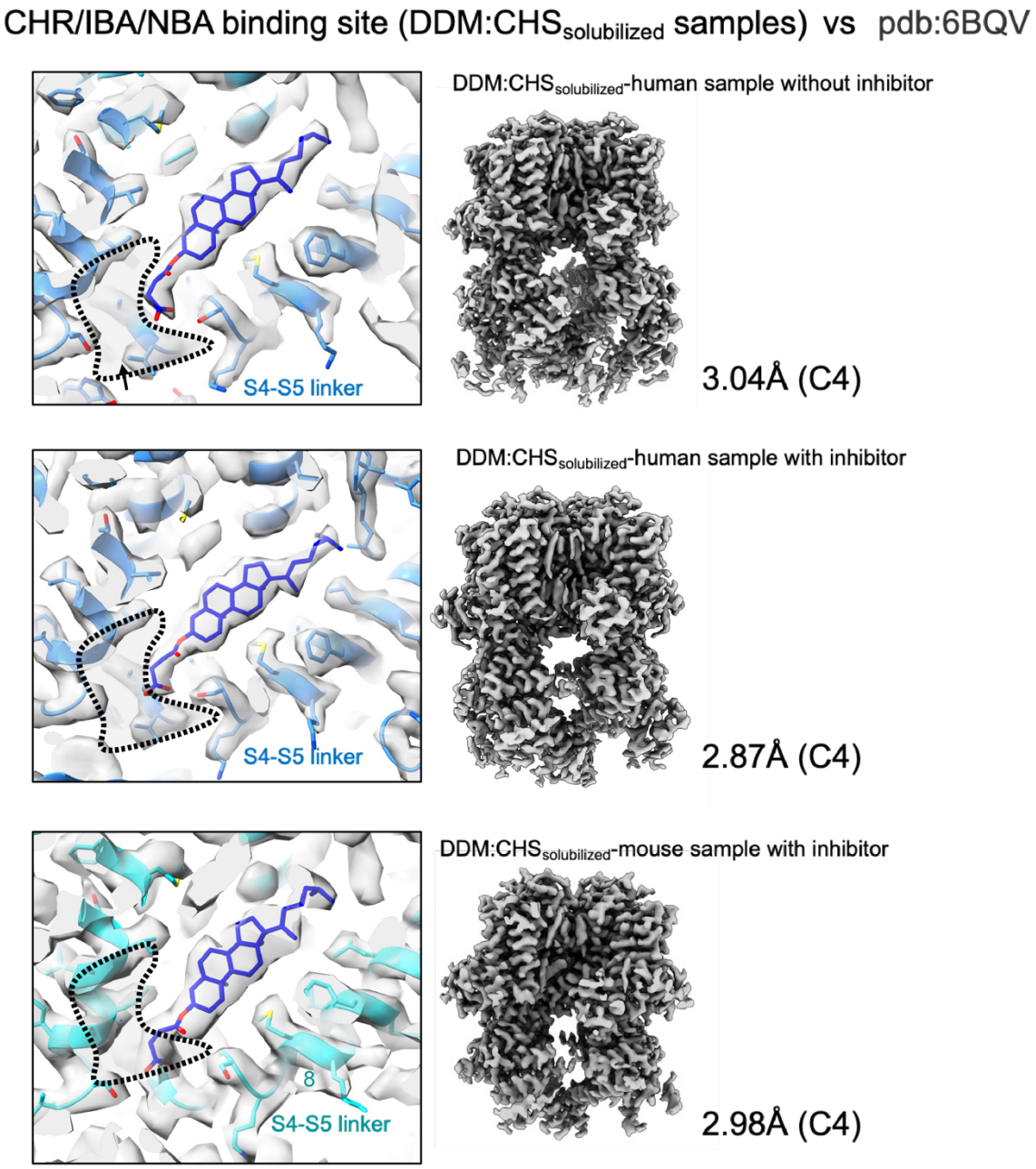

Supplementary Fig. 3: Cryo-EM maps of detergent-solubilized TRPM4 generated in this study highlight the presence of CHS in the drug binding site when fitted with the published model (pdb-id; 6BQV). The dashed line indicates the location of the drug-binding site determined in this study.

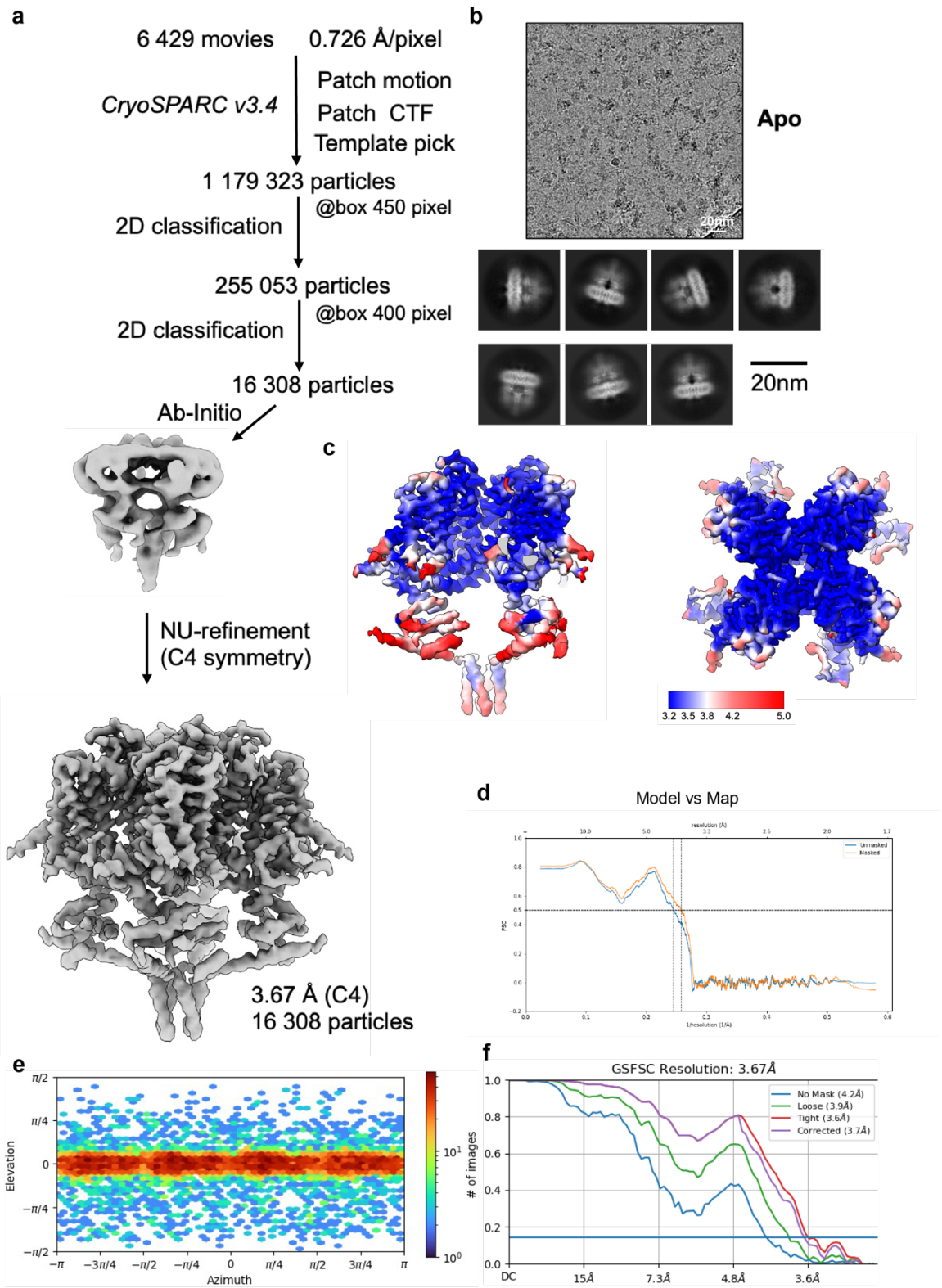

Supplementary Fig. 4: Cryo-EM data processing workflow and map resolution (a) The

391 image processing workflow of $HsTRPM4_{apo}$. (b) micrograph and 2D classes (c) Local

392 resolution (d) Model vs map FSC curves. (e) particle direction distribution. (f) FSC curves.

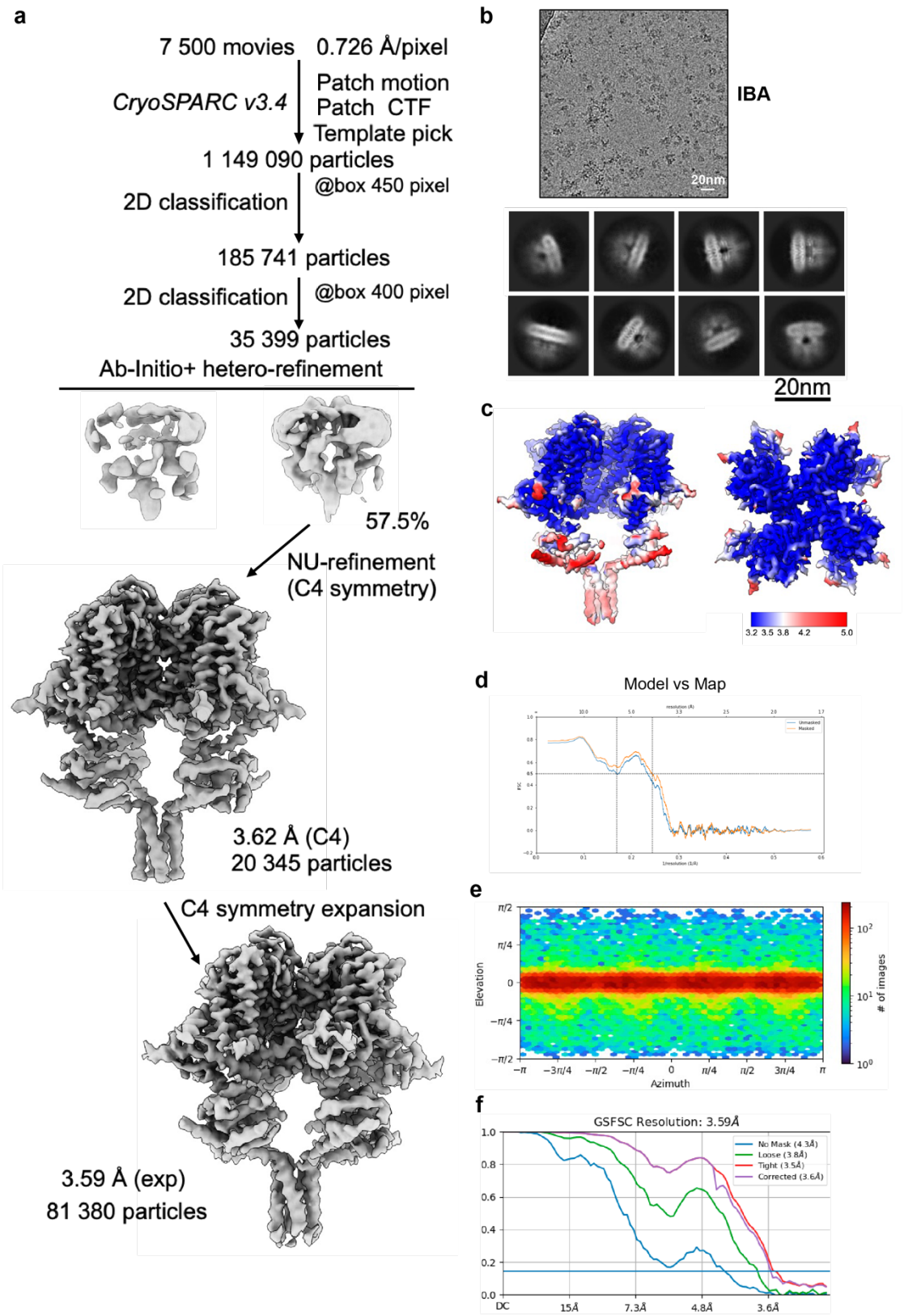

Supplementary Fig. 5: Cryo-EM data processing workflow and 3D reconstructions (a) The

image processing workflow of $HsTRPM4_{IBA}$. (b) Micrograph and 2D classes. (c) Local resolution. (d) Model vs map FSC curves. (e) Particle direction distribution. (f) FSC curves.

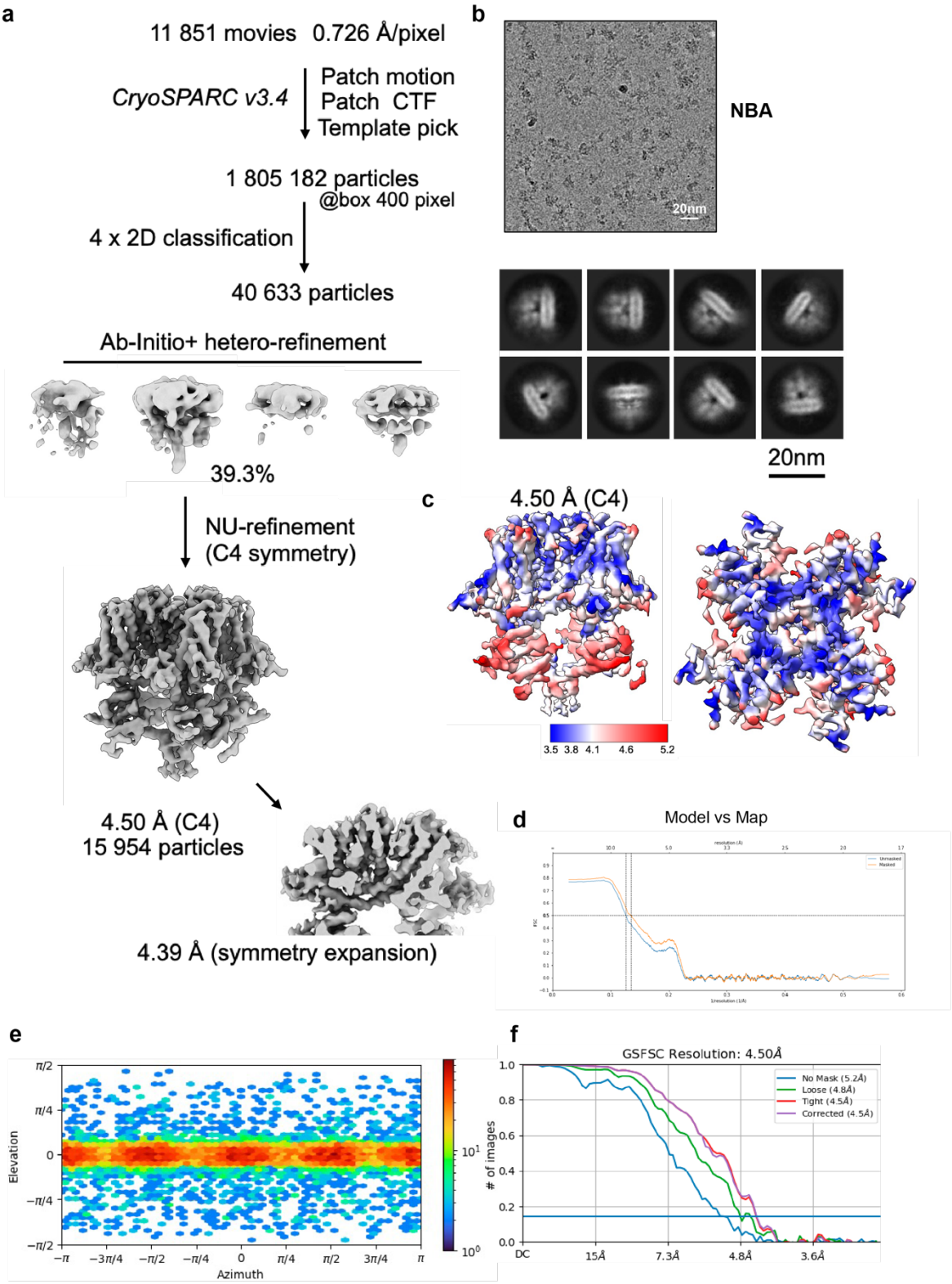

Supplementary Fig. 6: Cryo-EM data processing workflow and 3D reconstructions. (a) The image processing workflow of HsTRPM4$_{NBA}$. (b) Micrograph and 2D classes. (c) Local resolution. (d) Model vs. map FSC curves. (e) Particle direction distribution. (f) FSC curves.

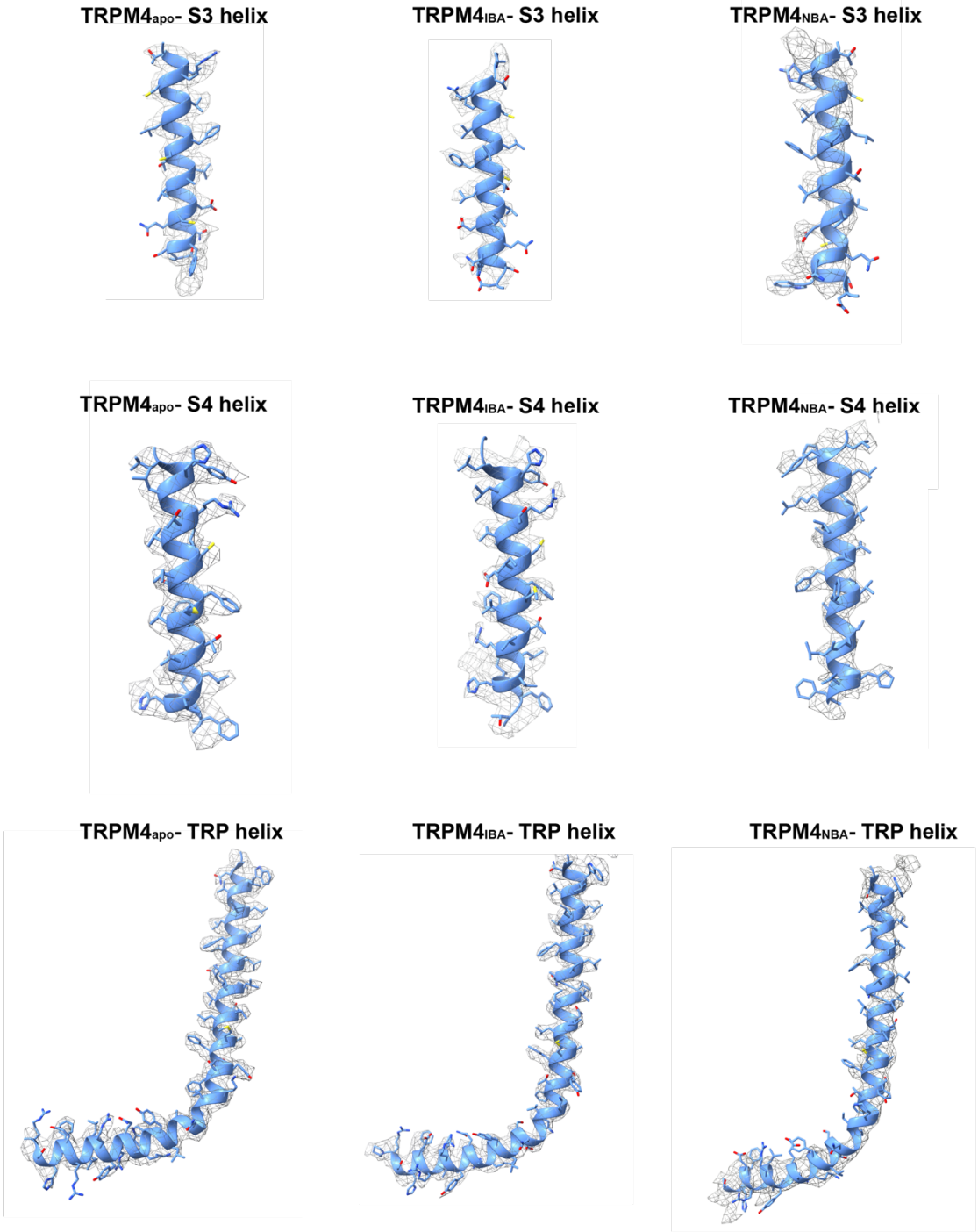

Supplementary Fig. 7: Zoom-in view of the cryo-EM maps of structural elements HsTRPM4$_{apo}$, HsTRPM4$_{IBA}$ and HsTRPM4$_{NBA}$.

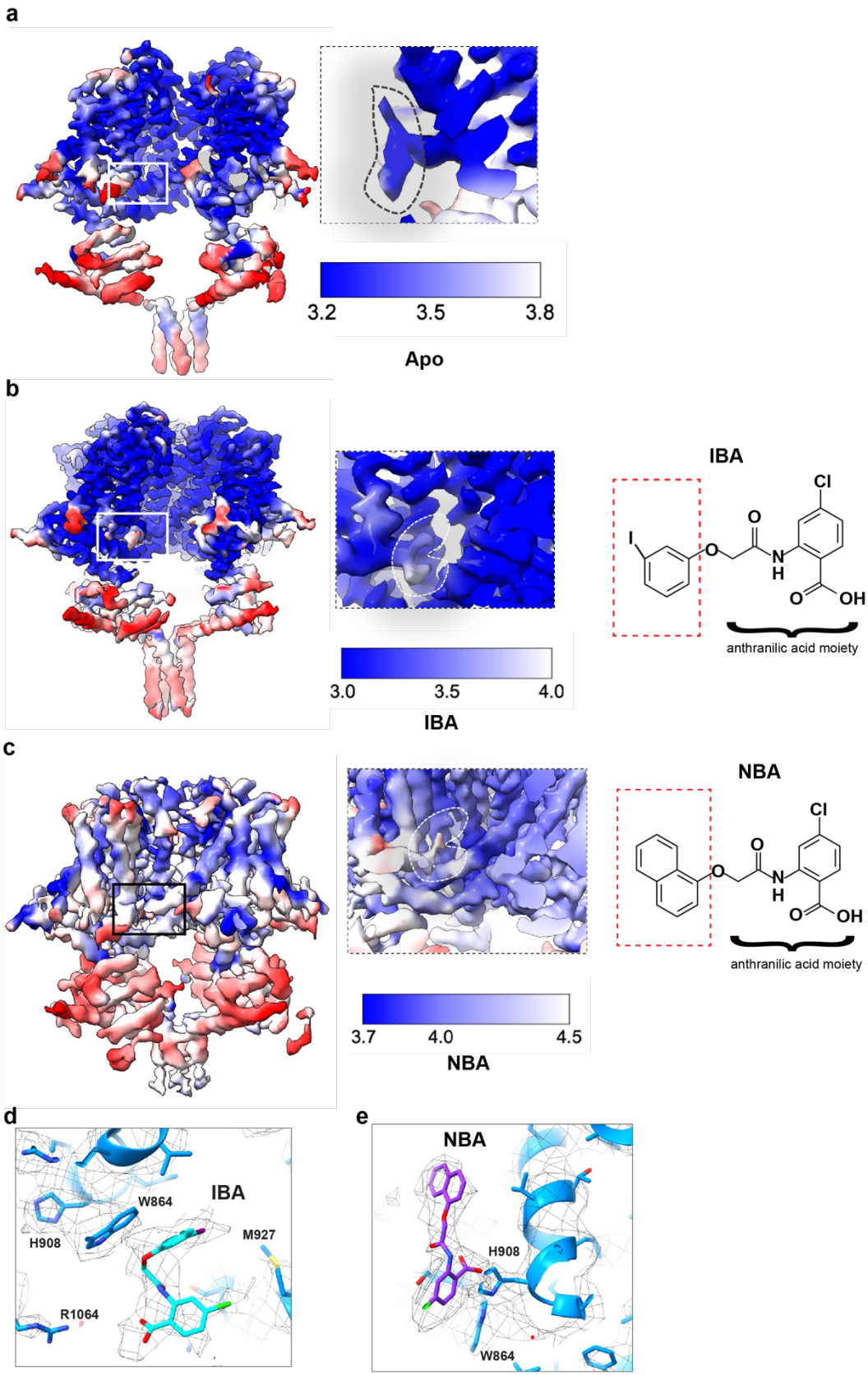

Supplementary Fig. 8: Local resolution maps of SMA solubilized HsTRPM4 generated in this study. (a) Map for the HsTRPM4$_{apo}$ with the density contained in the drug binding site

407 highlighted. (b) Map for $HsTRPM4_{IBA}$ with the density contained in the drug binding site
408 highlighted. The chemical structure of IBA is shown on the right. (c) Map for $HsTRPM4_{NBA}$ with
409 the density contained in the drug binding site highlighted. The chemical structure of the NBA
410 is shown on the right. (d and e) Zoom-in of NBA and IBA with the cryo-EM density in mesh
411 representation in different views compared to Figure 2 e and f.

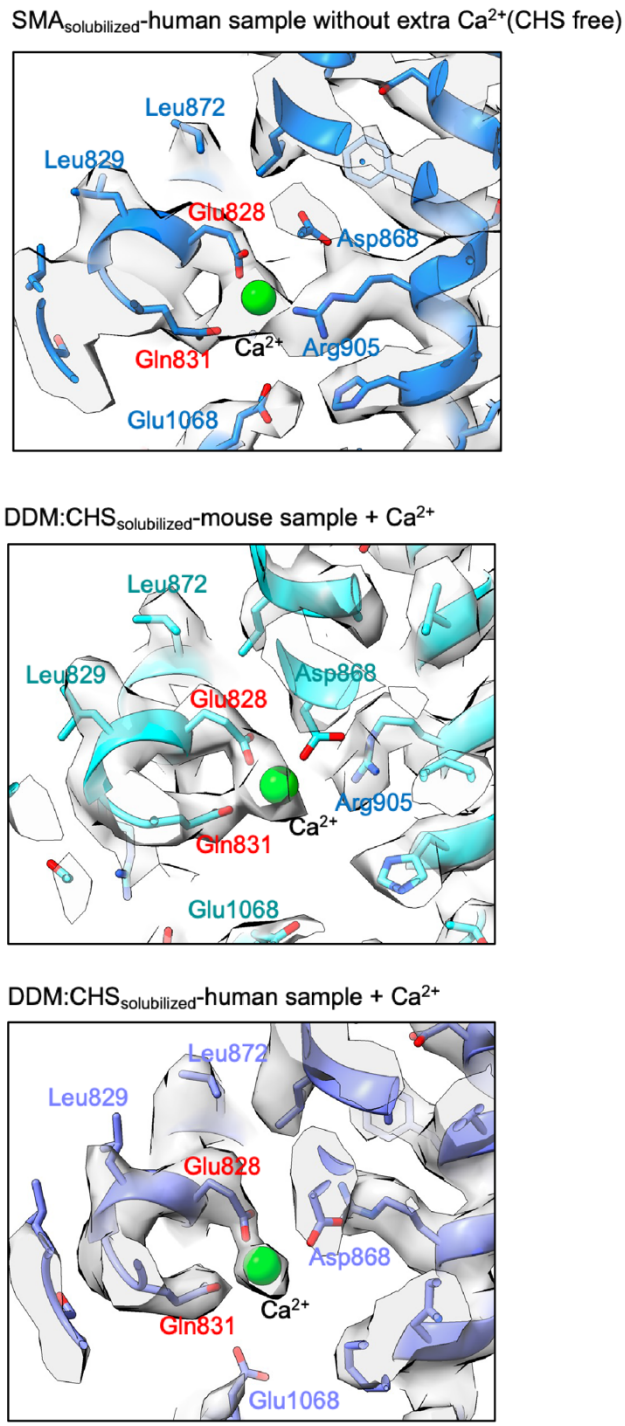

Supplementary Fig. 9: Identification of cryo-EM densities for Ca^{2+} ions in the maps generated in this study. The published HsTRPM4 model (pdb-id: 6BQV) is fitted into each map. Clear density is observed for Ca^{2+} in the map for the SMA solubilized human TRPM4 sample without the addition of extra calcium, which is comparable to the density shown for detergent-solubilized mouse and human TRPM4 with calcium added to the sample.

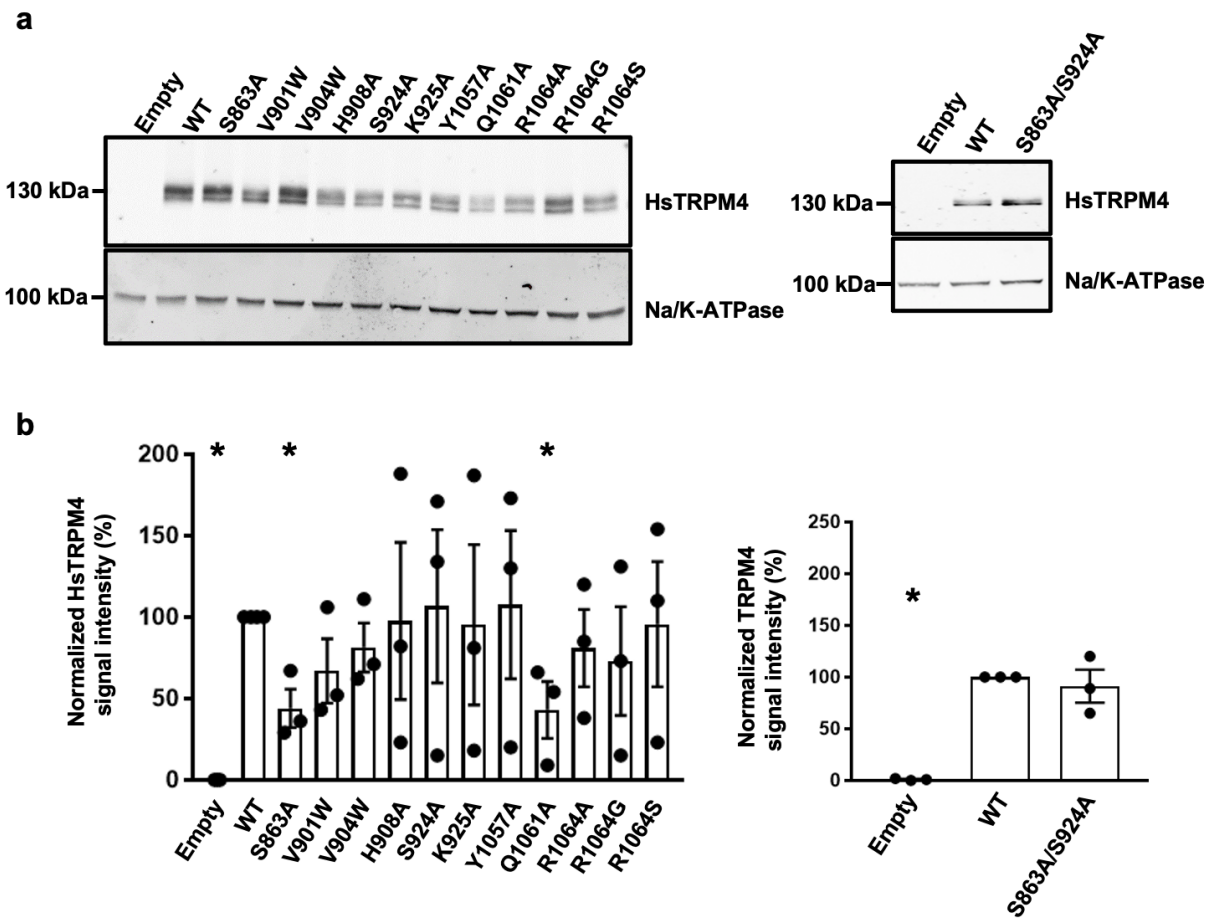

Supplementary Fig. 10: Expression of HsTRPM4 variants. (a) Western blot showing the expression of wildtype (WT) and HsTRPM4 variants expressed in HEK293 cells. (b) Graphical plot of relative western blot intensities between wildtype (WT) and HsTRPM4 variants. (*) represents the p-value <0.05 compared to the wildtype condition.

a

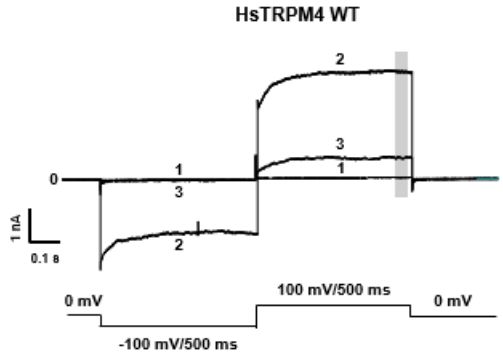

b

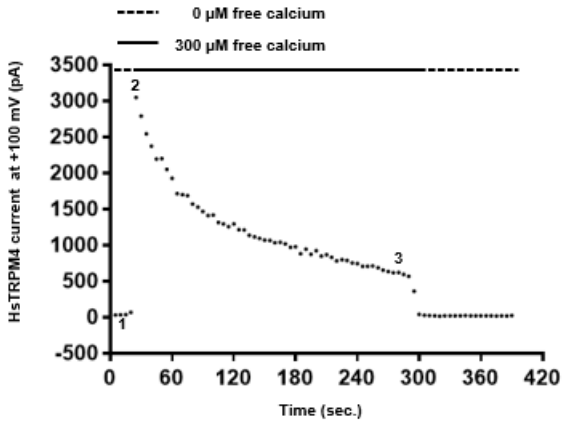

Supplementary Fig. 11: Time course of wildtype calcium-activated sodium current for HsTRPM4. (a) Example of raw traces (currents) from three different time points 1, 2, and 3 from the time course shown in (b) recorded from one cell expressing HsTRPM4 channels. Without free calcium (time point 1 in (b)), no calcium-activated sodium current is recordable at -100 mV or +100 mV (trace n°1 in (a)). Perfusion of 300 µM of free calcium concentration leads to the rapid activation of the channel (time point 2 in (b)), and a calcium-activated sodium current is recordable (trace n°2 in (a)) at both voltages (-100 mV and +100 mV). Following this quick activation, a rapid run-down of the calcium-activated sodium current mediated by the HsTRPM4 channel, due to the depletion of the PIP2 element, is observable until the current reaches stability (time point 3 in (b)). After the run-down, the calcium-activated sodium current amplitude is quantified by calculating the amplitude of this current

during the last 100 ms at +100 mV (grey zone in (a)). As depicted in trace number 3 in (a), the run-down is generally more pronounced at -100 mV, leading to almost a complete inhibition of the calcium-activated sodium current at this voltage.

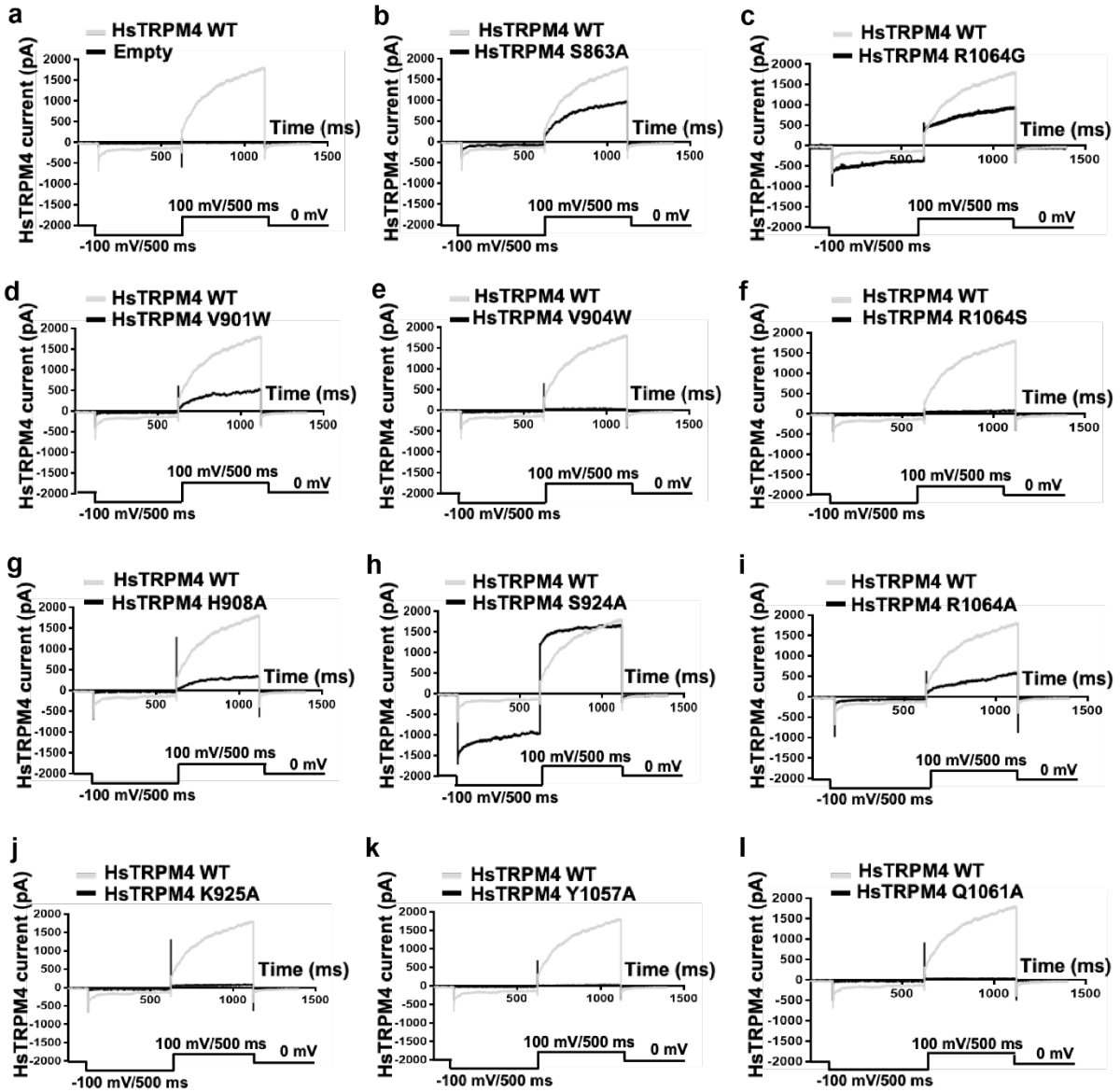

Supplementary Fig. 12: Calcium-activated sodium currents for HsTRPM4. (a to l) Representative traces of wildtype (WT, gray traces) and variants HsTRPM4 currents (black traces): S863A, V901W, V904W, H908A, S924A, K925A, Y1057A, Q1061A, R1064A, R1064G, and R1064S. Calcium-activated sodium currents for HsTRPM4 variant channels are generally smaller than WT currents, as depicted in Figure 3e, due to the amino acid alteration.

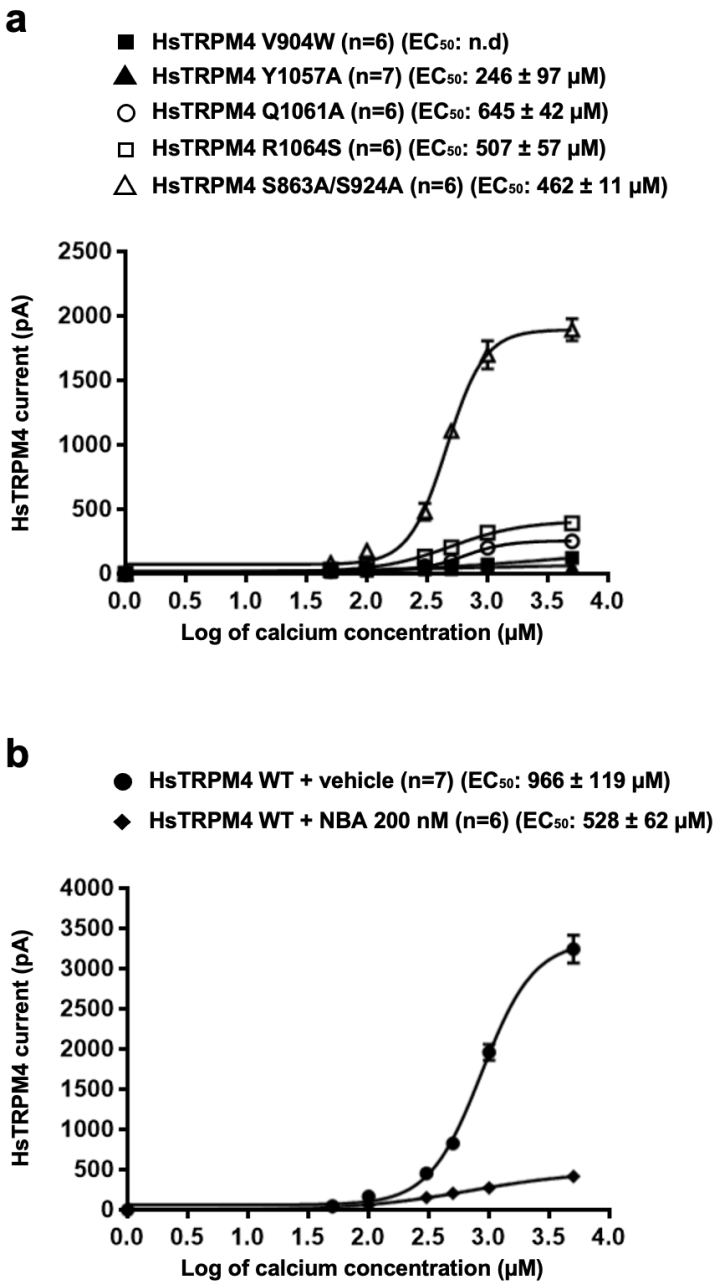

Supplementary Fig. 13: Calcium sensitivity curves of wildtype and variant HsTRPM4. (a) Calcium sensitivity curves of a few loss-of-function HsTRPM4 variants. (n): number of cells. n.d: not determinable. (b) Effect of NBA (200 nM) on the calcium sensitivity on wildtype (WT) HsTRPM4 channels.

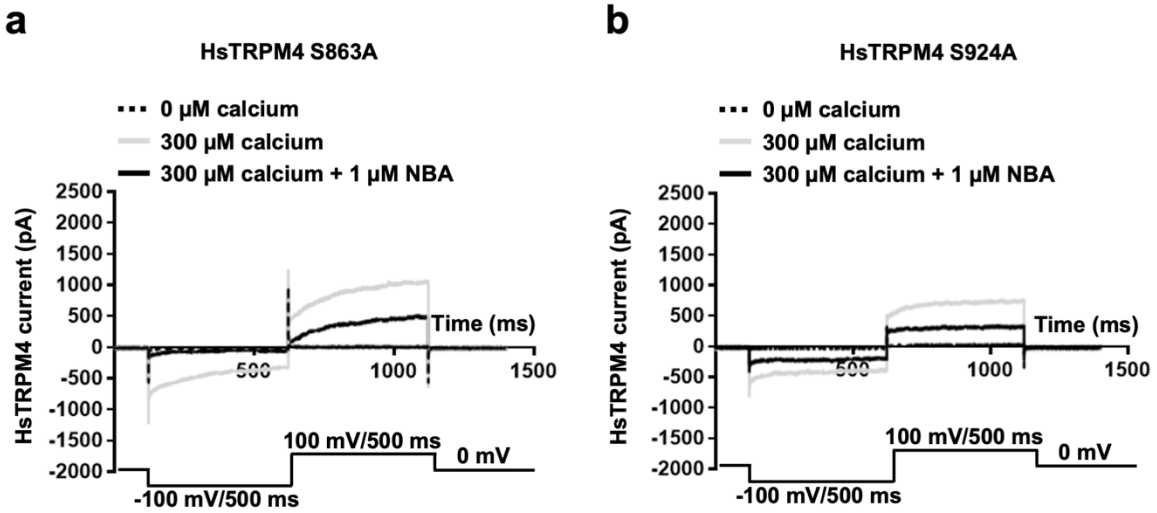

Supplementary Fig. 14: Calcium-activated sodium currents from HsTRPM4 channels. (a and b) Representative traces of variants HsTRPM4 current: S863A and S924A in the absence of free calcium in the solution (dotted black line), in the presence of 300 µM of free calcium concentration (grey line), and in the presence of 300 µM of free calcium concentration and 1 µM NBA (black line).

456 **References**

457 1. Clapham, D. E. TRP channels as cellular sensors. *Nature* **426**, 517–524 (2003).

458 2. Song, M. Y. & Yuan, J. X.-J. Introduction to TRP channels: structure, function, and
459 regulation. *Adv. Exp. Med. Biol.* **661**, 99–108 (2010).

460 3. Koivisto, A.-P., Belvisi, M. G., Gaudet, R. & Szallasi, A. Advances in TRP channel drug
461 discovery: from target validation to clinical studies. *Nat. Rev. Drug Discov.* **21**, 41–59
462 (2022).

463 4. Fallah, H. P. *et al.* A Review on the Role of TRP Channels and Their Potential as Drug
464 Targets_An Insight Into the TRP Channel Drug Discovery Methodologies. *Front.*
465 *Pharmacol.* **13**, 914499 (2022).

466 5. Launay, P. *et al.* TRPM4 is a Ca2+-activated nonselective cation channel mediating cell
467 membrane depolarization. *Cell* **109**, 397–407 (2002).

468 6. Nilius, B. *et al.* Voltage dependence of the Ca2+-activated cation channel TRPM4. *J.*
469 *Biol. Chem.* **278**, 30813–30820 (2003).

470 7. Wang, C., Naruse, K. & Takahashi, K. Role of the TRPM4 Channel in Cardiovascular
471 Physiology and Pathophysiology. *Cells* **7**, (2018).

472 8. Guinamard, R., Demion, M. & Launay, P. Physiological roles of the TRPM4 channel
473 extracted from background currents. *Physiology* **25**, 155–164 (2010).

474 9. Cheng, H. *et al.* TRPM4 controls insulin secretion in pancreatic beta-cells. *Cell Calcium*
475 **41**, 51–61 (2007).

476 10. Bianchi, B., Ozhathil, L. C., Medeiros-Domingo, A., Gollob, M. H. & Abriel, H. Four
477 TRPM4 Cation Channel Mutations Found in Cardiac Conduction Diseases Lead to
478 Altered Protein Stability. *Front. Physiol.* **9**, 177 (2018).

479 11. Liu, H. *et al.* Gain-of-function mutations in TRPM4 cause autosomal dominant isolated
480 cardiac conduction disease. *Circ. Cardiovasc. Genet.* **3**, 374–385 (2010).

481 12. Liu, H. *et al.* Molecular genetics and functional anomalies in a series of 248 Brugada
482 cases with 11 mutations in the TRPM4 channel. *PLoS One* **8**, e54131 (2013).

483 13. Janin, A. *et al.* TRPM4 mutations to cause autosomal recessive and not autosomal
484 dominant Brugada type 1 syndrome. *Eur. J. Med. Genet.* **62**, 103527 (2019).
485 14. Stallmeyer, B. *et al.* Mutational spectrum in the Ca(2+)--activated cation channel gene
486 TRPM4 in patients with cardiac conductance disturbances. *Hum. Mutat.* **33**, 109–117
487 (2012).
488 15. Hof, T. *et al.* TRPM4 non-selective cation channel variants in long QT syndrome. *BMC*
489 *Med. Genet.* **18**, 31 (2017).
490 16. Borgström, A., Peinelt, C. & Stokłosa, P. TRPM4 in Cancer—A New Potential Drug
491 Target. *Biomolecules* **11**, 229 (2021).
492 17. Zhao, Y., McVeigh, B. M. & Moiseenkova-Bell, V. Y. Structural Pharmacology of TRP
493 Channels. *J. Mol. Biol.* **433**, 166914 (2021).
494 18. Guinamard, R., Hof, T. & Del Negro, C. A. The TRPM4 channel inhibitor 9-phenanthrol.
495 *Br. J. Pharmacol.* **171**, 1600–1613 (2014).
496 19. Arullampalam, P. *et al.* Species-Specific Effects of Cation Channel TRPM4 Small-
497 Molecule Inhibitors. *Front. Pharmacol.* **12**, 712354 (2021).
498 20. Ozhathil, L. C. *et al.* Identification of potent and selective small molecule inhibitors of the
499 cation channel TRPM4. *Br. J. Pharmacol.* **175**, 2504–2519 (2018).
500 21. Guinamard, R., Simard, C. & Del Negro, C. Flufenamic acid as an ion channel
501 modulator. *Pharmacol. Ther.* **138**, 272–284 (2013).
502 22. Ruan, Z. *et al.* Structures of the TRPM5 channel elucidate mechanisms of activation
503 and inhibition. *Nat. Struct. Mol. Biol.* **28**, 604–613 (2021).
504 23. Zhao, C. *et al.* Structures of a mammalian TRPM8 in closed state. *Nat. Commun.* **13**,
505 3113 (2022).
506 24. Su, N. *et al.* Structural mechanisms of TRPV2 modulation by endogenous and
507 exogenous ligands. *Nat. Chem. Biol.* **19**, 72–80 (2023).
508 25. Guo, J. *et al.* Structures of the calcium-activated, non-selective cation channel TRPM4.
509 *Nature* **552**, 205–209 (2017).
510 26. Autzen, H. E. *et al.* Structure of the human TRPM4 ion channel in a lipid nanodisc.

Science **359**, 228–232 (2018).

27. Winkler, P. A., Huang, Y., Sun, W., Du, J. & Lü, W. Electron cryo-microscopy structure of a human TRPM4 channel. *Nature* **552**, 200–204 (2017).
28. Duan, J. *et al.* Structure of full-length human TRPM4. *Proc. Natl. Acad. Sci. U. S. A.* **115**, 2377–2382 (2018).
29. Dörr, J. M. *et al.* The styrene-maleic acid copolymer: a versatile tool in membrane research. *Eur. Biophys. J.* **45**, 3–21 (2016).
30. Syam, N. *et al.* Variants of Transient Receptor Potential Melastatin Member 4 in Childhood Atrioventricular Block. *J. Am. Heart Assoc.* **5**, (2016).
31. Smith, A. A. A. *et al.* Lipid Nanodiscs via Ordered Copolymers. *Chem* **6**, 2782–2795 (2020).
32. Hu, J. *et al.* Physiological temperature drives TRPM4 ligand recognition and gating. *Nature* **630**, 509–515 (2024).
33. Yin, Y. *et al.* Structural basis of cooling agent and lipid sensing by the cold-activated TRPM8 channel. *Science* **363**, (2019).
34. Wang, L. *et al.* Structures and gating mechanism of human TRPM2. *Science* **362**, (2018).

529 **Methods**

530 **Synthesis of 4-Chloro-2-(2-(3-iodophenoxy)acetamido)benzoic acid (IBA)**

531 *General Remarks*

532 Reagents and organic solvents were purchased from commercial suppliers and used without
533 further purification. Deionized water produced in-house or commercially available Milli-Q®
534 water was used depending on the application. Aqueous solutions of sodium hydroxide,
535 hydrogen chloride, saturated ammonium chloride, and saturated sodium chloride (brine)
536 were prepared with deionized water. Thin layer chromatography (TLC) was performed using
537 Macherey-Nagel ALUGRAM® Xtra SIL G/UV_{254} plates coated with 0.20 mm silica gel 60
538 containing fluorescent indicator. High-pressure liquid chromatography (HPLC) was
539 performed using a Thermo Fisher Scientific UltiMate 3000 RSLCnano System composed of
540 a DIONEX UltiMate 3000 Pump, a DIONEX UltiMate 3000 Sampler, a DIONEX UltiMate
541 3000 Column Compartment, and a DIONEX UltiMate 3000 Diode Array Detector. HPLC
542 measurements were conducted using Milli-Q® water (+ 0.1 % TFA) and acetonitrile (+ 0.1 %
543 TFA) as eluents and an Acclaim™ 120 C18 column (Thermo Scientific™). Flash column
544 chromatography (LC) was performed using the Teledyne Isco Combi*Flash*©*Rf*+ system.
545 Teledyne Isco Redi*Sep*©*Rf* dry load cartridges were used to prepare dry loads. If not stated
546 otherwise, dry loads were prepared on silica gel. Teledyne Isco Silica Redi*Sep*©*Rf*
547 prepacked silica flash columns of two sizes (24g and 80g) were used. Nuclear magnetic
548 resonance spectroscopy (NMR) was performed at the Department of Chemistry,
549 Biochemistry, and Pharmaceutical Sciences, Universität Bern (Furrer Group) using a Bruker
550 AVANCE III HD 300 GA spectrometer with a magnetic field of 7.05 Tesla and operating
551 frequencies of 300.13 MHz for ^{1}H measurements and 75.48 MHz for ^{13}C measurements.
552 High-resolution mass spectrometry (HRMS) was performed by the mass spectrometry
553 service (Schürch group) at the Department of Chemistry, Biochemistry and Pharmaceutical
554 Sciences, Universität Bern. The measurements were performed using electrospray
555 ionization (ESI) and a ThermoScientific LTQ Orbitrap XL mass spectrometer with high mass
556 resolution ($m/\Delta m$ > 100’000) and accuracy (Δm < 3ppm). The previously published synthetic

procedure (Ozhathil *et al*., 2018) to generate similar anthranilic anilide compounds was slightly adapted.

Methyl 4-chloro-2-(2-chloroacetamido) benzoate

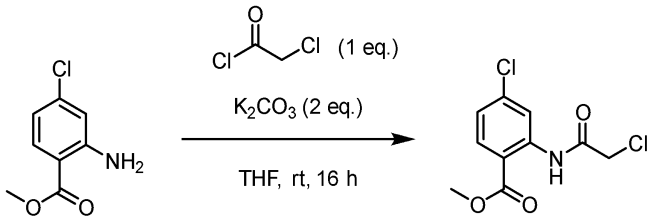

Methyl 2-amino-4-chlorobenzoate (1.7876 g, 9.6308 mmol) and potassium carbonate (2.6620 g, 19.2616 mmol, 2 eq.) were dissolved in tetrahydrofuran (150 mL) and stirred for 10 minutes at room temperature. Not all potassium carbonate dissolved completely. The mixture was then cooled in an ice bath, and chloroacetyl chloride (1.0919 g, 9.6676 mmol, 0.77 mL, 1 eq.) was added dropwise via a syringe. This mixture was stirred at 0 °C for 10 minutes and further stirred at room temperature for 16 hours. The reaction mixture showed a pale pink color and was monitored by thin layer chromatography (eluent: cyclohexane /ethyl acetate, 4:1). After full conversion of the starting material, water was added to the reaction mixture and the product was extracted with ethyl acetate. The combined organic phases were then washed with brine, dried over magnesium sulfate, filtered through celite, and the volatiles were evaporated under reduced pressure. The crude pale-yellow and solid product was purified by flash column chromatography (eluent: cyclohexane /ethyl acetate, gradient from 0 % to 20 % ethyl acetate). The product (white powder) was dried *in vacuo*. Yield Methyl 4-chloro-2-(2-chloroacetamido) benzoate quant., 2.5 g, 9.5387 mmol. ^{1}H NMR (300 MHz, DMSO-d_6) δ 11.44 (s, 1H), 8.52 (d, J = 2.2 Hz, 1H), 8.00 (d, J = 8.6 Hz, 1H), 7.33 (dd, J = 8.6, 2.2 Hz, 1H), 4.48 (s, 2H), 3.89 (s, 3H). ^{13}C NMR (75 MHz, DMSO-d_6) δ 166.75, 165.67, 140.29, 138.75, 132.51, 123.77, 119.84, 115.57, 52.82, 43.35. HRMS (ESI) *m/z* $[M+H]^+$ calculated for $C_{10}H_9Cl_2NO_3$ 262.0032, found 262.0037.

Methyl 4-chloro-2-(2-(3-iodophenoxy)acetamido)benzoate

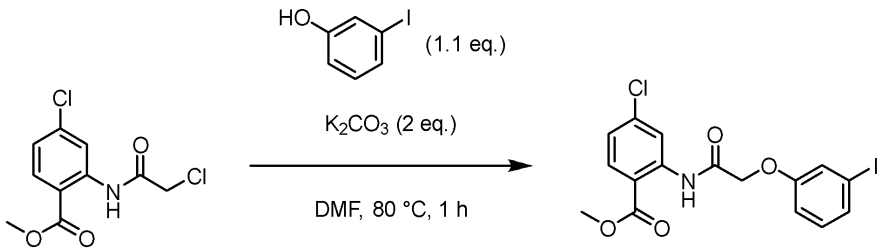

Methyl 4-chloro-2-(2-chloroacetamido) benzoate (0.3270 g, 1.2475 mmol) was dissolved in dimethylformamide (6 mL), and potassium carbonate (0.3465 g, 2.5073 mmol, 2 eq.) was added. This mixture was stirred for 10 minutes at room temperature. Not all potassium carbonate dissolved completely. 3-Iodophenol (0.3019 g, 1.3723 mmol, 1.1 eq.) was then dissolved in dimethylformamide (6 mL) and added via syringe to the reaction mixture, which was stirred at 80 °C. The color of the reaction mixture changed to deep brown. The reaction was monitored by thin layer chromatography (eluent: cyclohexane /ethyl acetate, 4:1). Upon full conversion of the starting material after 60 minutes, water was added to the mixture, resulting in a brown and cloudy suspension. The product was extracted with ethyl acetate, and the combined organic phases were then washed with brine, dried over magnesium sulfate, filtered through celite, and the volatiles were evaporated under reduced pressure. The crude product was purified by flash column chromatography (eluent: cyclohexane /ethyl acetate, gradient from 0 % to 20 % ethyl acetate), and the purified product (white powder) was dried *in vacuo*. Yield Methyl 4-chloro-2-(2-(3-iodophenoxy)acetamido)benzoate 84 %, 0.4653 g, 1.0442 mmol. ^{1}H NMR (300 MHz, DMSO-d_6) δ 11.76 (s, 1H), 8.70 (d, J = 2.1 Hz, 1H), 8.01 (d, J = 8.6 Hz, 1H), 7.48 (t, J = 1.9 Hz, 1H), 7.40 (ddd, J = 6.4, 2.5, 1.6 Hz, 1H), 7.30 (dd, J = 8.6, 2.2 Hz, 1H), 7.15 – 7.09 (m, 2H), 4.79 (s, 2H), 3.91 (s, 3H). ^{13}C NMR (75 MHz, DMSO-d_6) δ 167.24, 166.87, 157.61, 140.57, 138.94, 132.56, 131.50, 130.66, 123.67, 123.34, 119.33, 114.75, 114.64, 95.04, 67.35, 52.76. HRMS (ESI) *m/z* $[M+H]^+$ calculated for $C_{16}H_{13}ClINO_4$ 445.9651, found 445.9647.

604 *4-Chloro-2-(2-(3-iodophenoxy)acetamido)benzoic acid (IBA)*

605 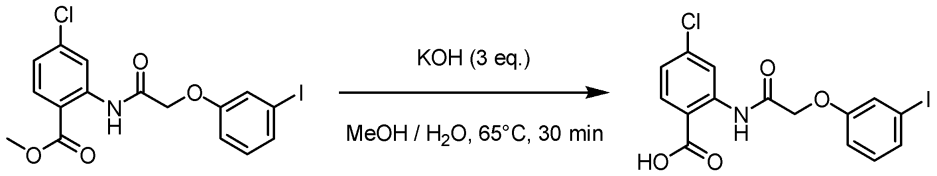

606 Methyl 4-chloro-2-(2-(3-iodophenoxy)acetamido)benzoate (0.4531 g, 1.0168 mmol) was
607 dissolved in methanol (100 mL) and potassium hydroxide (0.1744 g, 3.1075 mmol, 3 eq.)
608 was dissolved in Milli-Q® water (20 mL). The aqueous potassium hydroxide solution was
609 added to the reaction mixture, which was stirred at 65° C, and progress was monitored by
610 thin layer chromatography (eluent: dichloromethane /methanol, 9:1). Upon full conversion of
611 the starting material after 30 minutes, the reaction mixture was cooled down to room
612 temperate. Aqueous hydrochloric acid solution (1 M, ca. 100 mL) was then added, resulting
613 in immediate precipitation of the product, which was filtered off using a glass filter frit (Por.
614 4), and the solid white product was dried *in vacuo*. Yield 4-Chloro-2-(2-(3-
615 iodophenoxy)acetamido)benzoic acid 79 %, 0.3466 g, 0.8030 mmol. Purity (HPLC): 98.52 %
616 (at 254 nm). ^{1}H NMR (300 MHz, DMSO-d_6) δ 14.08 (s, 1H), 12.25 (s, 1H), 8.77 (d, J = 2.1
617 Hz, 1H), 8.03 (d, J = 8.6 Hz, 1H), 7.46 (m, 1H), 7.38 (dt, J = 7.0, 1.7 Hz, 1H), 7.27 (dd, J =
618 8.6, 2.2 Hz, 1H), 7.19 – 7.08 (m, 2H), 4.77 (s, 2H). ^{13}C NMR (75 MHz, DMSO-d_6) δ 168.78,
619 167.24, 157.58, 141.12, 138.69, 133.05, 131.48, 130.55, 123.74, 123.06, 118.78, 114.94,
620 114.29, 95.06, 67.21. HRMS (ESI) *m/z* $[M-H]^-$ calculated for $C_{15}H_{11}ClINO_4$ 429.9349, found
621 429.9348.

622

623 **Description of drugs**

624 Stock solutions of 4-chloro-2-(2-(naphthalene-1-yloxy)acetamido)benzoic acid (NBA) and the
625 iodo-modified congener; 4-chloro-2-(2-(3-iodo-phenoxy)acetamino)benzoic acid (IBA) were
626 dissolved in 100% DMSO to a final concentration of 10 mM. IBA was synthesized to
627 increase the electron densities when using the cryo-EM approaches. Although, as proof of
628 concept, only NBA has been used in the functional experiments presented in this study, the
629 inhibitory efficacity of IBA has been evaluated and is the same as of NBA. NBA and IBA

630 solutions were freshly made before each experiment. The lipophilicity of these drugs (cLog
631 *P*) has been calculated using the algorithms on Swiss ADME from the Swiss Institute of
632 Bioinformatics (http://www.swissadme.ch/). The Log *P* corresponds to the compound's
633 concentration ratio at equilibrium between organic (octanol) and aqueous phases. A
634 negative Log *P* means the compound is hydrophilic, and a positive value for Log *P* denotes a
635 more lipophilic compound. At pH = 7.4, the NBA and IBA compounds (both protonated
636 (carboxylic acid) and deprotonated (carboxylate) forms) tend to be lipophilic. NBA is slightly
637 more lipophilic than IBA (consensus cLog *P* protonated/deprotonated: NBA: 3.59/3.32; IBA:
638 3.25/3.05). The decadic $\log_{10}$ is used here.
639
640 **Plasmid constructs design and cloning**
641
642 For this study, the wild-type codon-optimized *H. sapiens* (Hs) and *M. musculus* (Mm)
643 TRPM4 genes coding full-length TRPM4 were synthesized, fused to consecutive C-terminal
644 HA (hemagglutinin)—and FLAG-tags, and cloned into a pCDNA-3.1 plasmid for expression
645 in HEK293 cells by the CMV (cytomegalovirus) promoter (GenScript Biotech). Mutant
646 variants were generated by site-directed mutagenesis (GenScript Biotech).
647
648 **Protein expression and purification**
649 The full-length *H. sapiens* TRPM4 and *M. musculus* TRPM4 were expressed and purified
650 from HEK293F cells grown in suspension. For expression, HEK293F cells were transfected
651 with 1 mg of a plasmid containing the TRPM4 gene per liter of cells using PEI
652 (polyethylenimine). The cultures were grown at 37°C and 5% CO_2 for 48 hours. The cultures
653 were harvested by centrifugation at 3,000 xg for 30 mins at 4°C and washed in 1x PBS,
654 followed by another round of centrifugation. The pellets were carefully resuspended in lysis
655 buffer containing HEPES-NaOH, pH 7.5, 200 mM NaCl and supplemented with cOmplete™
656 EDTA-free Protease Inhibitor Cocktail (Roche). 4 tablets of protease inhibitor cocktail were
657 added per 100ml of buffer. Following resuspension, the cells were lysed by sonication for a
658 total of 1 min in 10 sec On and OFF cycles and an amplitude of 35%. After sonication, the

659 membrane fraction was harvested by centrifugation using an Optima XPN-100
660 ultracentrifuge (Beckman Coulter) with the Ti45 rotor and spun at 70,560 × g for 30 minutes
661 at 4°C. The resulting pellets were stored at -80°C. For solubilization of the membrane
662 fraction with SMALP200, 12 g of pellet was resuspended in 30 ml of solubilization buffer
663 containing HEPES-NaOH, pH 7.5, 200 mM NaCl and 0.5% SMALP200 (CubeBiotech
664 GmbH) supplemented with 2 tablets of cOmplete™ EDTA-free Protease Inhibitor Cocktail
665 (Roche). The resuspended pellet was homogenized manually in a 40 ml Kimble glass
666 homogenizer (Sigma). The tube containing the mixture was then placed in a bottle with a stir
667 bar and left to incubate at 4°C for 1 hour 30 mins. The homogenate was clarified by
668 centrifugation for 30 min at 70,560 × *g* at 4°C in an Optima XPN Ultracentrifuge (Beckman
669 Coulter) using a Ti-45 rotor. The supernatant, which contained soluble FLAG-tagged
670 HsTRPM4 mixed with 1ml of Anti-FLAG® M2 affinity gel (Millipore, Billerica, MA) pre-
671 equilibrated with wash buffer containing 25 mM HEPES-NaOH, pH 7.5, 200 mM NaCl. The
672 beads were washed with 100 mL of wash buffer containing 25 mM HEPES-NaOH, pH 7.5,
673 200 mM NaCl and eluted with 4 mL elution buffer containing 25 mM HEPES-NaOH, pH 7.5,
674 200 mM NaCl, 120 µg/ml of 3xFLAG peptide, followed by concentration on 100 K Amicon
675 Ultra-15 concentrators (Millipore, Billerica, MA) to an absorbance at 280 nm of 1.0 to prepare
676 cryo-EM grids.
677 For detergent solubilization, 12 g of pellet was resuspended in 30 ml of solubilization buffer
678 containing HEPES-NaOH, pH 7.5, 200 mM NaCl, 1% n-Dodecyl-beta-Maltoside (DDM) and
679 0.1% Cholesteryl Hemissucinate (CHS)
680 (Avanti Pola lipids) supplemented with 2 tablets of cOmplete™ EDTA-free Protease Inhibitor
681 Cocktail (Roche). The resuspended pellet was homogenized manually in a 40 ml Kimble
682 glass homogenizer (Sigma). The tube containing the mixture was then placed in a bottle with
683 a stir bar and left to incubate at 4°C for 2 hours. The homogenate was clarified by
684 centrifugation for 30 min at 70,560 × *g* at 4°C in an Optima XPN Ultracentrifuge (Beckman
685 Coulter) using a Ti-45 rotor. The supernatant, which contains soluble FLAG-tagged
686 HsTRPM4 mixed with 1ml of Anti-FLAG® M2 affinity gel (Millipore, Billerica, MA) pre-

687 equilibrated with wash buffer containing 25 mM HEPES-NaOH, pH 7.5, 200 mM NaCl and
688 1% DDM/ 0.1% CHS. The beads were washed with 100 mL of wash buffer containing 25 mM
689 HEPES-NaOH, pH 7.5, 200 mM NaCl, and 1% DDM/ 0.1% CHS and eluted with 4 mL
690 elution buffer containing 25 mM HEPES-NaOH, pH 7.5, 200 mM NaCl, 120 µg/ml of 3xFLAG
691 peptide and 1% DDM/ 0.1% CHS. The purified protein was run on a Superose 6 gel filtration
692 column pre-equilibrated with 0.005% Lauryl Maltose Neopentyl Glycol (LMNG)/ 0.0005%
693 CHS and the peak fraction was concentrated on 100 K Amicon Ultra-15 concentrators
694 (Millipore, Billerica, MA) to an absorbance at 280 nm of 1.0 to prepare cryo-EM grids.
695
696 **SDS-PAGE Analysis**
697 An SDS-PAGE analysis was performed to assess the purity of purified proteins. 15 µL of
698 protein sample was supplemented with 5 µL of 4X NuPAGE LDS Sample Buffer (Thermo
699 Scientific). Samples were incubated at 95°C for 10 minutes before loading on 4-12%
700 SurePAGE™ Bis-Tris precast gels (Witec AG). Spectra™ Prestained Protein Ladder
701 (Thermo Scientific) (10 to 180 kDa) was also loaded on the gel to run as a size marker. Gels
702 were run in 1X Tris-MOPS SDS running buffer (Witec AG) at 200 V for 30 minutes, washed
703 briefly in MilliQ water, and stained for 2 hours with QuickBlue Protein Stain (LuBioScience
704 GmbH) with shaking. Gels were washed in MilliQ water before imaging on an iBright FL1500
705 Imaging System (Thermo Scientific).
706
707 **Cryo-EM sample preparation and data collection**
708 Purified TRPM4 was incubated with a final concentration of 0.2mM IBA for $TRPM4_{IBA}$ and
709 NBA for $TRPM4_{NBA}$ for 30 mins at room temperature before freezing cryo-EM grids. Cryo-EM
710 grids were prepared by applying 3 µl of concentrated sample onto 400-mesh R1.2/1.3
711 UltrAuFoil grids (Quantifoil Micro Tools GmbH), which had rendered hydrophilic by glow
712 discharging at 15mA for 60seconds with a PELCO EasyGlow device (TED PELLA, INC).
713 The samples were immediately blotted and plunged frozen into liquid ethane using a Vitrobot

714 Mark IV plunge freezer (Thermo Fisher Scientific). Cryo-EM data were collected using the
715 automated data acquisition software EPU (Thermo Fisher Scientific) on a Titan Krios G4
716 transmission electron microscope (Thermo Fisher Scientific), operating at 300kV and
717 equipped with a cold-FEG electron source, a SelectrisX energy filter and a Falcon4 direct
718 detection camera. Images were recorded in counting mode at a nominal magnification of
719 165kx, corresponding to a physical pixel size of 0.726 Å at the sample level. Datasets were
720 collected at a defocus range of 0.8 to 2.5 µm with a total electron dose of 60 $e^-/Å^2$. Image
721 data were saved as Electron Event Recordings (EER).
722
723 **Cryo-EM image processing, model building, and refinement**
724 The cryo-EM image processing was performed using cryoSPARC v3.4 [34].
725 Patch-based motion correction (cryoSPARC implementation) was used to align the EM
726 movie stacks and apply dose-dependent resolution weighting to recorded movies. CTF
727 estimation was performed using the patch-based option as well. For the data of the
728 $HsTRPM4_{apo}$, a total of 6,429 movies at 0.726 Å per pixel were collected, and 1000 particles
729 were manually picked and used for one round of 2D classification for template creation.
730 Template-based automated particle picking was then used on the recorded image data,
731 which resulted in a set of 1'719'323 particles at a size of 450 pixels. Two rounds of 2D
732 classification were performed for the initial step of particle cleaning, resulting in 255'053
733 particles in the first round and 16'308 in the second round. Ab initio and non-uniform
734 refinement yielded one 3D reconstruction with a map at 3.67 Å overall resolution in C4
735 symmetry (**Supplementary Fig. 4**).
736
737 For the data of the $HsTRPM4_{IBA}$, a total of 7,500 movies at 0.726 Å per pixel were collected.
738 2D classes from the $HsTRPM_{apo}$ dataset were used for template-based picking. Template-
739 based automated particle picking resulted in a set of 1'149'090 particles at a size of 450
740 pixels. Two rounds of 2D classification were performed for the initial step of particle cleaning,
741 resulting in 185'741 particles at 400 pixels in the first round and 35'399 particles in the

742 second round. Ab initio and hetero-refinement refinement yielded two 3D reconstructions.
743 One reconstruction representing 57.5% of particles was selected for further non-uniform
744 refinement, resulting in a map at 3.62 Å overall resolution in C4 symmetry. Following
745 symmetry expansion, the overall resolution of the map could be improved to an overall
746 resolution of 3.62 Å (**Supplementary Fig. 5**).
747
748 For the data of the $HsTRPM4_{NBA}$, a total of 11,851 movies at 0.726 Å per pixel were
749 collected. 2D classes from the $HsTRPM_{apo}$ dataset were used for template-based picking.
750 Template-based automated particle picking resulted in a set of 1'805'182 particles at 400
751 pixels. Four rounds of 2D classification were performed for the initial step of particle
752 cleaning, resulting in 40'633 particles. Ab initio and hetero-refinement refinement yielded
753 four 3D reconstructions. One reconstruction representing 15'954 particles was selected for
754 further non-uniform refinement, resulting in a map at 4.50 Å overall resolution in C4
755 symmetry from 15,954 particles (**Supplementary Fig. 6**).
756
757 Cryo-EM data was also collected for DDM/CHS solubilized mouse and human TRPM4.
758 MmTRPM4 data was collected with 5mM Calcium chloride present in the sample. Two
759 datasets were collected for DDM/CHS solubilized HsTRPM4 with 5mM Calcium chloride
760 present in one sample and both 5mM calcium chloride and 0.2mM NBA present in the other.
761 Details of the data collection are included (**Supplementary Table 2**).
762
763 Atomic models for $HsTRPM_{apo}$, $HsTRPM4_{IBA}$, and $HsTRPM4_{NBA}$ structures were mainly built
764 in Coot 0.9.4 [35], using a model PDB id: 6BQV as an initial model. Real-space refinement for
765 all built models was performed using Phenix, version 1.19.2-4158, by applying a general
766 restraints setup [33].
767
768 **Cell Culture**

769 TsA-201 cells were cultured with Dulbecco's Modified Eagle's culture Medium DMEM
770 (Gibco, Basel, Switzerland) supplemented with 10% FBS, 0.5% penicillin, and streptomycin
771 (10,000 U/mL) at 37°C in a 5% CO_2 incubator.
772
773 **Transfections**
774 Sixty mm dishes (BD Falcon, Durham, North Carolina, USA) at 80% of confluence were
775 transiently transfected using Xtreme Gene 9™ transfection reagent (Sigma Aldrich Merck,
776 Switzerland) and following the manufacturer's instructions. In brief, 1,000 ng of either empty
777 vector or HsTRPM4 WT or variants of HsTRPM4 (TRPM4 S863A, TRPM4 V901W, TRPM4
778 V904W, TRPM4 H908A, TRPM4 S924A, TRPM4 K925A, TRPM4 Y1057A, TRPM4 Q1061A,
779 TRPM4 R1064A, TRPM4 R1064G, TRPM4 R1064S or TRPM4 S863A/S924A) was mixed
780 with a solution containing 100 ng of a reporter gene coding for GFP and 1,000 ng of empty
781 vector. The expression of GFP was used to evaluate the transfection efficiency procedure,
782 and the empty vector was added to reach a certain amount of total cDNA to ensure an
783 efficient transfection. These final cDNA solutions (2,100 ng) were mixed with 210 µL of opti-
784 MEM (Gibco, Basel, Switzerland) and 6.3 µL of Xtreme Gen9™ reagent (ration 1/3). After 30
785 minutes at room temperature, the cDNA solutions were applied to the cells. Forty-eight hours
786 post-transfection, the cells were harvested for the western blot experiments.

787 **Western-blots**
788 The expression of the human TRPM4 channel was assessed in whole-cell lysates. First,
789 cells were washed with PBS 1X and then lysed for 1 hour at 4 °C in lysis buffer (50 mM
790 HEPES pH 7.4, 1.5 mM $MgCl_2$, 150 mM NaCl, 1 mM EGTA pH 8, 10% glycerol, 1% Triton X-
791 100, and Complete® protease inhibitor cocktail (Roche Diagnostics, Mannheim, Germany)).
792 The pellet was discarded after centrifugation at 4 °C, 16,000 g for 15 minutes. Protein
793 concentrations of each lysate sample were measured in triplicate by Bradford assay and
794 interpolated by a bovine serum albumin (BSA) standard curve. Samples were denatured at
795 30 °C for 37 minutes before loading on a gel. Twenty µg of protein for each sample was run

796 at 150 V for 1 hour on 9% polyacrylamide gels. The Turbo Blot dry blot system (Biorad,
797 Hercules, CA, USA) was used to transfer the samples to a nitrocellulose membrane. All
798 membranes were stained with Ponceau as a qualitative check for equivalent total protein
799 loading. Membranes were then rinsed twice with TBS 1X and blocked with 5% BSA in TBS
800 1X for 1 hour. After this blocking step, the membranes were incubated for 2 hours with rabbit
801 anti-human TRPM4 antibody (epitope: $_{1137}$CRDKRESDSERLKRTSQKV$_{1155}$, Pineda, Berlin,
802 Germany) diluted 1:1,000 in TBS 1X + 0.1% tween and mouse anti-Na^+/K^+ ATPase antibody
803 (Abcam ab 7671) diluted 1:1,000 in TBS 1X + 0.1% tween. The membranes were washed 4
804 times in TBS 1X + 0.1% tween before incubating with fluorescent secondary antibodies.
805 Secondary antibodies IR Dye 800 CW, anti-rabbit diluted (1:20,000) in TBS 1X + 0.1%
806 tween and IR Dye 700 CW, anti-mouse diluted (1:20,000) in TBS 1X + 0.1% tween (LI-COR
807 Biosciences, Lincoln, NE, USA) were added for 1 hour. After 4 washes with TBS 1X + 0.1%
808 tween and 3 washes in TBS 1X, membranes were scanned with the FUSION FX Spectra®
809 Infrared Imaging System (VILBER smart imaging, Marne-la-Vallée, France) to detect
810 fluorescent protein. Subsequent quantitative analysis of protein content was achieved by
811 measuring and comparing band densities (equivalent to fluorescence intensities of the
812 bands) using the *Evolution-Capt software* (VILBER smart imaging, Marne-la-Vallée, France).
813 The background was first subtracted for each band (human TRPM4 and Na^+/K^+ ATPase),
814 then TRPM4 intensity was divided by the intensity of the Na^+/K^+ ATPase band (for a given
815 sample) and normalized for comparison.

816 **Electrophysiology**

817 **Transfections**

818 Thirty-five mm dishes (BD Falcon, Durham, North Carolina, USA) at 80% of confluence were
819 transiently transfected using JetPEI™ transfection reagent (Polyplus transfection, Illkirch,
820 France) and following the instructions of the manufacturer. In brief, 500 ng of either empty
821 vector or HsTRPM4 WT or variants of HsTRPM4 (HsTRPM4 T677I, HsTRPM4 S863A,
822 HsTRPM4 V901W, HsTRPM4 V904W, HsTRPM4 H908A, HsTRPM4 S924A, HsTRPM4

823 K925A, HsTRPM4 Y1057A, HsTRPM4 Q1061A, HsTRPM4 R1064A, HsTRPM4 R1064G,
824 HsTRPM4 R1064S or HsTRPM4 S863A/S924A) was mixed with 200 ng of a reporter gene
825 coding for GFP. Expression of GFP was used to identify transfected cells during patch clamp
826 experiments. Coding DNAs (cDNAs from HsTRPM4 and GFP) were mixed with 4 µl of
827 JetPEI™ and 46 µl of 150 mM NaCl. After 15 minutes at room temperature, the cDNA
828 solutions were applied to the cells. Twenty-four hours post-transfection, the cells were plated
829 at low density in a new 35 mm dish coated with poly-l-lysine. The cells were patched 24
830 hours post-platting (48 hours post-transfection).
831
832 **Inside-out patch clamp**
833 Electrophysiological recordings were performed in the inside-out patch-clamp configuration
834 with patch pipettes (1 and 2 µm tip opening) pulled from 1.5 mm borosilicate glass capillaries
835 (Zeitz-Instruments GmbH, München, Germany) using micropipette puller P 97 (Sutter
836 Instruments, Novato, CA, United States). The tips were polished for 2–4 MΩ pipette
837 resistance in the bath solution. The pipette solution contained 150 mM NaCl, 10 mM
838 HEPES, and 2 mM $CaCl_2$ (pH 7.4 with NaOH). The initial bath solution with a concentration
839 of 0 µM of free calcium contained 150 mM NaCl, 10 mM HEPES, and 2 mM HEDTA (pH 7.4
840 with NaOH). After reaching the inside-out configuration, different solutions were perfused at
841 the intracellular side of the membrane patch using a modified rapid solution exchanger
842 (Perfusion Fast-Step SF-77B; Warner Instruments Corp. CT, United States).
843 For calcium sensitivity experiments. The first solution, applied for 3 to 5 sweeps to reach a
844 stable current, is the bath solution (150 mM NaCl, 10 mM HEPES, and 2 mM HEDTA; pH
845 7.4 with NaOH) with a concentration of 0 µM of free calcium. Then, to activate TRPM4
846 channels, a solution (150 mM NaCl, 10 mM HEPES; pH 7.4 with NaOH) containing different
847 concentrations of free calcium (0 µM, 50 µM, 100 µM, 300 µM, 500 µM, 1000 µM, 5000 µM)
848 was applied. The effect of the calcium was quantified when the sodium current of the
849 calcium-activated HsTRPM4 reached stability. Finally, the bath solution with a concentration

850 of 0 μM of free calcium was used to quantify the potential leak current that can occur during
851 such recordings.
852 For drug dose-response experiments. The first solution, applied for 3 to 5 sweeps to reach
853 the stable current, is the bath solution (150 mM NaCl, 10 mM HEPES, and 2 mM HEDTA;
854 pH 7.4 with NaOH) with a concentration of 0 μM of free calcium. Then, after stabilization of
855 the current, a solution (150 mM NaCl, 10 mM HEPES; pH 7.4 with NaOH) containing a
856 concentration of 300 μM free calcium without compounds was applied to activated
857 HsTRPM4 channels and recorded the sodium current of the calcium-activated HsTRPM4
858 until its stabilization. Then, a solution (150 mM NaCl, 10 mM HEPES; pH 7.4 with NaOH)
859 containing a concentration of 300 μM of free calcium and the compound at different
860 concentrations (10 nM, 50 nM, 100 nM, 500 nM, 1000 nM, 5000 nM, 10’000 nM, 50’000 nM)
861 were applied. The drug's effect was quantified when the sodium current of the calcium-
862 activated HsTRPM4 reached stability. Finally, the bath solution with a concentration of 0 μM
863 of free calcium was used to quantify the potential leak current that may occur during such
864 recordings. No investigation and comparison have been made concerning the kinetics of
865 block and washout, and only ‘’stable’’ currents have been used to calculate the percentage
866 of inhibition.
867 The sodium current of the calcium-activated HsTRPM4 was recorded with a Multiclamp
868 700B amplifier (Molecular Devices, Sunnyvale, CA, United States) controlled by Clampex 10
869 via Digidata 1332A (Molecular Devices, Sunnyvale, CA, United States). Data were low-pass
870 filtered at 5 kHz and sampled at 10 kHz. Experiments were performed at room temperature
871 (20–25°C). The holding potential was 0 mV. The stimulation protocol consisted of two pulses
872 totaling 1’000 ms for measuring steady-state currents repeated at 0.2Hz (1 sweep every 5
873 sec.). The first pulse was at −100 mV for 500 ms, and the second was at +100 mV for
874 500 ms. For analysis, the effect of the compounds on calcium-activated sodium current
875 HsTRPM4 has been calculated by averaging the values of this current during the last
876 100 ms of the second sweep (at +100 mV) on the trace recorded during the stable phase.
877 Due to the stronger run-down observable at -100 mV (first pulse of the stimulation protocol)

878 for the HsTRPM4 channels leading to, after stabilization of the current, at sometimes almost
879 no sodium current quantifiable at -100 mV of the calcium-activated HsTRPM4 channel
880 (supplementary Figure 11b, trace number 3 at -100 mV), the effects of the compounds at -
881 100 mV have not been quantified. Electrophysiology data were exported and analyzed using
882 Prism7.05 GraphPad™ software (GraphPad by Dotmatics, San Diego, CA, USA).
883 Concentration-response curves were fitted using the log(inhibitor) vs. response-variable
884 slope (four parameters) equation (Y=Bottom + (Top-Bottom)/(1+10^((LogIC50-X)
885 *HillSlope))) where X corresponds to the log of concentration and Y current recorded in pA.
886 The decadic $\log_{10}$ is used here.

887 **Data analyses and statistics**

888 Data are represented as means ± SEM. Statistical analyses were performed using
889 Prism7.05 GraphPad™ software (GraphPad by Dotmatics, San Diego, CA, USA). An
890 unpaired Mann-Whitney U test was used to compare two unpaired groups. $p < 0.05$ was
891 considered significant. No muti-group comparison has been performed in this study. Western
892 blots were done in triplicate, and at least 6 cells were used for different doses in
893 electrophysiology experiments. Important information. Due to the limited channels available
894 in our perfusion system (7 channels available), only 5 different concentrations for
895 compounds (NBA or IBA) could be applied to the same cells (the 2 remaining channels were
896 used for the solution with a concentration of 0 µM of free calcium without no compounds to
897 record the background current not related to the activation of HsTRPM4 and the solution
898 with a concentration of 300 µM of free calcium with no compounds to activate the HsTRPM4
899 channel and record the calcium-activated sodium current). Not all the concentrations (8 in
900 total) for compounds presented in the different figures have been applied to the same cell.
901 This limitation did prohibit the determination of the IC_{50s} per cell; otherwise, the fundamental
902 statistical rule of independence would be violated. Consequently, IC_{50s} were calculated
903 based on the average data point collected for x cells per concentration, as presented in the
904 different figures, and no statistical analysis between the different conditions was performed

905 on those variables. However, a two-way ANOVA with two-factor repeated measures was
906 used to investigate any statistical difference of inhibition, mediated by the compounds,
907 between WT and variant conditions at 1μM of a compound, a concentration close to the
908 general IC_{50s} of the variants investigated. The percentages of inhibition for all variants,
909 except the TRPM4 T677I, at the concentration of 1μM of a compound, significantly differed
910 ($p<0.05$) from the WT and are smaller, suggesting a decrease of inhibition, mediated by the
911 compounds, on these variants of HsTRPM4 channel.
912
913 **Data visualization**
914 Gel images were processed and prepared on ImageJ (Version 1.53k). Figures were
915 rendered using PyMOL, (The PyMOL Molecular Graphics System, version 1.8.2.0,
916 Schrödinger, LLC), UCSF Chimera, UCSF ChimeraX [36], and Adobe Illustrator
917 (https://adobe.com/products/illustrator).
918
919 **Data and Code Availability**
920 The reconstructed maps are available from the EMDB database under access codes
921 HsTRPM4apo (EMD-19057), $HsTRPM4_{IBA}$ (EMD-19061), $HsTRPM4_{NBA}$ (EMD-19069) (EMD-
922 19060, local). The atomic models are available in the PDB database, access codes
923 HsTRPM4apo (PDB 8RCR), $HsTRPM4_{IBA}$ (8RCU) and $HsTRPM4_{NBA}$ (PDB 8RD9).
924
925
926 **Methods-only references**
927 35. Punjani, A., Rubinstein, J. L., Fleet, D. J. & Brubaker, M. A. cryoSPARC: algorithms
928 for rapid unsupervised cryo-EM structure determination. *Nat. Methods* **14**, 290–296
929 (2017).
930 36. Emsley, P., Lohkamp, B., Scott, W. G. & Cowtan, K. Features and development of
931 Coot. *Acta Crystallogr. D Biol. Crystallogr.* **66**, 486–501 (2010).
932 37. Liebschner, D. *et al.* Macromolecular structure determination using X-rays, neutrons

933 and electrons: recent developments in Phenix. *Acta Crystallogr D Struct Biol* **75**,
934 861–877 (2019).
935 38. Goddard, T. D. *et al.* UCSF ChimeraX: Meeting modern challenges in visualization
936 and analysis. *Protein Sci.* **27**, 14–25 (2018).

937